Geochemistry Geophysics Geosystems G3

Article
Volume 12, Number 7
8 July 2011
Q07004, doi:10.1029/2011GC003567
ISSN: 1525-2027

Published by AGU and the Geochemical Society

Discretization errors and free surface stabilization in the finite difference and marker-in-cell method for applied geodynamics: A numerical study

T. Duretz, D. A. May, T. V. Gerya, and P. J. Tackley

Institute of Geophysics, Department of Earth Sciences, ETH Zürich, Zurich CH-8093, Switzerland (thibault.duretz@erdw.ethz.ch)

[1] The finite difference–marker-in-cell (FD-MIC) method is a popular method in thermomechanical modeling in geodynamics. Although no systematic study has investigated the numerical properties of the method, numerous applications have shown its robustness and flexibility for the study of large viscous deformations. The model setups used in geodynamics often involve large smooth variations of viscosity (e.g., temperature-dependent viscosity) as well large discontinuous variations in material properties (e.g., material interfaces). Establishing the numerical properties of the FD-MIC and showing that the scheme is convergent adds relevance to the applications studies that employ this method. In this study, we numerically investigate the discretization errors and order of accuracy of the velocity and pressure solution obtained from the FD-MIC scheme using two-dimensional analytic solutions. We show that, depending on which type of boundary condition is used, the FD-MIC scheme is a second-order accurate in space as long as the viscosity field is constant or smooth (i.e., continuous). With the introduction of a discontinuous viscosity field characterized by a viscosity jump (η^*) within the control volume, the scheme becomes first-order accurate. We observed that the transition from second-order to first-order accuracy will occur with only a small increase in the viscosity contrast ($\eta^* \approx 5$). We have employed two methods for projecting the material properties from the Lagrangian markers onto the Eulerian nodes. The methods are based on the size of the interpolation volume (4-cell, 1-cell). The use of a more local interpolation scheme (1-cell) decreases the absolute velocity and pressure discretization errors. We also introduce a stabilization algorithm that damps the potential oscillations that may arise from quasi free surface calculations in numerical codes that employ the strong form of the Stokes equations. This correction term is of particular interest for topographic modeling, since the surface of the Earth is generally represented by a free surface. Including the stabilization enables physically meaningful solutions to be obtained from our simulations, even in cases where the time step value exceeds the isostatic relaxation time. We show that including the stabilization algorithm in our FD stencil does not affect the convergence properties of our scheme. In order to verify our approach, we performed time-dependent simulations of free surface Rayleigh-Taylor instability.

Components: 14,800 words, 14 figures, 3 tables.

Keywords: convergence; finite difference; free surface; marker-in-cell.

Index Terms: 0545 Computational Geophysics: Modeling (1952, 4255, 4316); 0560 Computational Geophysics: Numerical solutions (4255); 3225 Mathematical Geophysics: Numerical approximations and analysis (4260).

Received 16 February 2011; **Revised** 6 May 2011; **Accepted** 7 May 2011; **Published** 8 July 2011.

Duretz, T., D. A. May, T. V. Gerya, and P. J. Tackley (2011), Discretization errors and free surface stabilization in the finite difference and marker-in-cell method for applied geodynamics: A numerical study, *Geochem. Geophys. Geosyst.*, *12*, Q07004, doi:10.1029/2011GC003567.

1. Introduction

1.1. Background

[2] Unravelling the deformation history from the present-day geological record is a challenging problem. To complement field data and traditional interpretation based geodynamic modeling approaches, mathematical models are often employed to develop our understanding of geological processes. The use of thermomechanical models which solve the equations of conservation of momentum, mass and energy has a long history in geodynamics.

[3] In these models one prescribes (1) a set of mathematically permissible boundary conditions, (2) the geometry of the model domain, and (3) the geometry and rheology (or lithology) of the rocks to be modeled. Using such an approach to simulate geologically realistic scenarios is complicated by several attributes which we discuss in more detail. At a given length scale, rocks can be extremely heterogenous. Here, the heterogeneities may consist of differing lithology, or in simply the contrast of effective material properties (viscosity, shear modulus, etc). Furthermore, the contrast of effective material properties may be extremely large, and occur over a very small length scale. The geometry of the heterogeneities is also a complex issue to treat in thermomechanical models as coherent structures (e.g., layering) may need to be represented. Over geological time scales, rocks are subjected to enormous strains, i.e., large deformation. Given that rocks possess characteristics of both ductile and brittle materials (over a certain time scale), during their deformation they will yield. In contrast to many engineering applications, geologists are interested in the deformation modes both prefailure and postfailure.

[4] This set of physical attributes associated with geological processes has motivated numerous different modeling approaches. Rather than describe all the methods in detail, we instead provide a brief historical overview of the approaches and highlight the merits and shortcomings with regards to the physical attributes identified above. Two broad categories of methods can be defined: (a) those which explicitly models interfaces from which a material domain (volume) is inferred or (b) those which explicitly model volumes.

[5] We refer to *van Keken et al.* [1997], *Popov and Sobolev* [2008], *Zlotnik et al.* [2007], *Braun et al.* [2008], *Samuel and Evonuk* [2010], *Schmalzl and Loddoch* [2003], and *Lin and van Keken* [2006] as examples of methods from category (a). While many methods to represent interfaces exist, developing robust schemes with low numerical diffusion, and which are capable to representing complex structures required by geodynamic models is nontrivial. With the advent of affordable, distributed memory computer clusters, it is also an important consideration whether a given method can be implemented in 3-D and whether the algorithm is suitable to be implemented in a distributed memory environment.

[6] For geological applications, the geometric complexity of the structure needing to be represented, combined with algorithmic difficulties associated with implementing interface based models, has motivated the use of "particle based" methods (category (b)). The term "particles" is deliberately used vaguely as different methods may regard "particles" in different ways. In general, particles are used to represent a given lithology (i.e., material properties) and as such represent volumetric quantities. The huge advantage afforded by particle methods is that they are completely unstructured, and do not posses any connectivity associated with neighboring particles. The use of particles to track complex flow features (e.g., free surface evolution) dates back to the pioneering marker-and-cell (MAC) method [*Harlow and Welch*, 1965; *Pracht*, 1971]. Here, the particles (or markers) were Lagrangian quantities and were used to represent (discretize) the volume of the fluid. The fluid equations for conservation of mass and momentum were solved via a staggered grid, finite difference method. The markers were used to indicate which cells in the grid were completely filled with fluid, and which contained the free surface, and hence where the free surface boundary condition should be applied. The MAC methodology has been extensively developed in the geodynamics community [*Weinberg and Schmeling*, 1992; *Poliakov and Podladchikov*, 1992; *Zaleski and Julien*, 1992; *Fullsack*, 1995; *Tackley*, 1998; *Babeyko et al.*, 2002; *Gerya and Yuen*, 2003, 2007; *Moresi et al.*, 2003, 2007]. These authors follow the underlying concept introduced in the MAC scheme. Namely, the conservation equations are solved on a grid, while complex geometric features are represented with markers. In the geodynamic applications, the markers are not used simply to identify regions of free surface/fluid/air, rather they typically represent different lithologies to which material parameters and a constitutive law is attributed. Other Lagrangian particle based

methods used in geodynamics include *Poliakov et al.* [1993], *Braun and Sambridge* [1994, 1995], *Hansen* [2003], and *Schwaiger* [2007]. While different in their methodology, they embody Harlow's original concept.

[7] The idea of representing complex geometric structures via Lagrangian markers is very appealing, and consequently gained widespread usage in computational geodynamics for a number of reasons: it is very simple to associate lithology and material properties to markers; the numerical implementation of marker fields is algorithmically straight forward; three-dimensional implementations of marker methods are not significantly more complex than its 2-D counterpart; the approach is amenable to distributed memory environments.

1.2. Present Work

[8] To obtain reliable results from numerical models, one has to ensure that a sufficiently high "numerical resolution" is used to guarantee that the physics is captured. Depending on the method, numerical resolution might be related to the size of grid cell used in a mesh, or the number of markers used to represent a volume of fluid. Furthermore, one has to establish that the numerical error associated with the method used actually decreases if the resolution is increased. That is, the *convergence* of the method must be established. Understanding the convergence properties of a method provides some insight into the resolution required to resolve a certain flow feature (for example) and furthermore, it also indicates how rapidly the error is reduced as a function of increasing numerical resolution.

[9] Despite the widespread usage and acceptance of thermomechanical modeling as a viable tool to study geology, few studies focus on the accuracy of the numerical methods being employed. In general, it is often regarded that it is difficult to perform a formal error analysis on marker based methods due to their inherent unstructured nature. Furthermore, geological applications often utilize discontinuous material properties (e.g., viscosity). The use of spatially variable coefficients also make formal error analysis more complicated. While the marker-grid methods lack a formal error analysis, numerous numerical studies have been performed. Numerical studies consist of either output comparison between different codes or laboratory experiments (a.k.a. benchmark studies) [*Blankenbach et al.*, 1989; *Travis et al.*, 1990; *van Keken et al.*, 1997; *Tackley and King*, 2003; *Buiter et al.*, 2006; *Schmeling et al.*, 2008; *OzBench et al.*, 2008; *van Keken et al.*, 2008], or solution comparison between an analytic solution and the model output [*Moresi et al.*, 1996; *Deubelbeiss and Kaus*, 2008; *Popov and Sobolev*, 2008; *Zhong et al.*, 2008].

[10] Given the number of practitioners now employing marker grid style thermomechanical numerical models, it is important to thoroughly address the order of convergence of these methods, either through carefully designed numerical experiments or analytical approaches [*Nicolaides*, 1992; *Nicolaides and Wu*, 1996]. In this work, we consider one such representative marker grid based approach [*Gerya and Yuen*, 2003, 2007] and numerically examine the convergence properties of the method. This is achieved by using three different analytic solutions for a Stokes flow problem with continuous and discontinuous viscosity structures. Although idealized, these solutions have sufficient complexity in terms of their lithology and geometry to be regarded as representative of a typically geodynamic application. Using the analytic solutions, the true discretization error can be measured. While using analytic solutions to measure errors and determine the order of convergence is by no means exhaustive (in a mathematical sense), in the absence of formal convergence proof, the approach is justified if the analytic solutions possess sufficient complexity compared to the intended application of interest. Given the interest in representing free surfaces for modeling topography and the difficulties that are related to the introduction of this surface [*Kaus et al.*, 2010], we adopt a strong form variant of the stabilization technique described by *Kaus et al.* [2010] for a finite difference scheme. To verify that the use of this algorithm does not affect the convergence properties of our finite difference–marker-in-cell scheme (FD-MIC), we again utilize analytic solutions.

[11] The outline of this paper is as follows. In the first section we introduce the physical problem of interest along with the numerical method that we employ. In section 3 we describe the sources of errors and the methodology we employ to analyze the discretization error of our numerical method. The models used in the convergence study and the results obtained using the convergence properties of the FD-MIC method are described in the section 4. Section 5 provides an application of our method to solve a time-dependent free surface problem. In section 6 we discuss some future directions and perspectives beyond examining dis-

cretization errors within numerical schemes. Lastly, concluding remarks are provided in section 7.

2. Physical Problem and Numerical Method

2.1. Governing Equations

[12] Traditionally, the flow of geomaterials over geological timescales is calculated by solving the momentum equations neglecting inertial terms (Stokes equations)

$$\frac{\partial \sigma_{ij}}{\partial x_j} = -\rho g_i. \tag{1}$$

This equation describes the balance between the viscous force and the body forces for an infinitesimal volume of fluid. The viscous force is formulated as the gradient of the stress tensor (σ_{ij}) and the body force is written as the product of the fluid density (ρ) and the gravitational acceleration vector (g_i). Moreover, in the absence of melting and phase transitions, geodynamic flows are considered as incompressible. Incompressibility is enforced by coupling the aforementioned equations with the continuity equation

$$\frac{\partial v_i}{\partial x_i} = 0, \tag{2}$$

where v_i is the velocity and x_i is the spatial coordinate. Equations (1) and (2) are valid over the model domain which we denote by Ω. To close the system the equations for the conservation of momentum and mass are supplemented with two boundary conditions. Decomposing the boundary of Ω into two, nonoverlapping regions denoted by $\partial\Omega_N$ and $\partial\Omega_D$, the boundary conditions are written as

$$\sigma_{ij} n_j = a_i, \qquad \mathbf{x} \in \partial\Omega_N \tag{3}$$

and

$$v_i = b_i, \qquad \mathbf{x} \in \partial\Omega_D. \tag{4}$$

Here n_j is the outward point normal to the boundary of Ω, a_i is an applied traction and b_i is a prescribed velocity.

[13] The mechanical behavior of the material is defined by a constitutive relationship. We relate the stress tensor σ_{ij} to the strain rate tensor $\dot{\epsilon}_{ij}$, using a linear, isotropic viscous rheology given by

$$\sigma_{ij} = -p\delta_{ij} + 2\eta\dot{\epsilon}_{ij}, \tag{5}$$

where p is the pressure, η is the viscosity and the strain rate is given by

$$\dot{\epsilon}_{ij} = \frac{1}{2}\left(\frac{\partial v_i}{\partial x_j} + \frac{\partial v_j}{\partial x_i}\right). \tag{6}$$

[14] The model domain contains several different material compositions, or lithologies which we denote by $C(\mathbf{x})$. The compositional field C does not possess any physical diffusion, and evolves according to

$$\frac{\partial C}{\partial t} + v_i \frac{\partial C}{\partial x_i} = 0. \tag{7}$$

[15] Prior to any discretization, the equations above are nondimensionalized by means of dynamic scaling. This scaling is achieved by first defining a set of characteristic units such as a characteristic length (e.g., domain size), a characteristic time (e.g., diffusion time, inverse background strain rate), a characteristic viscosity (e.g., minimum viscosity in the domain) and secondly deriving all the related characteristic units (mass, stress, force..). In section 4, we employ characteristic units that are equal to 1. The results are not scaled back to dimensional units and therefore the velocity errors and pressure are dimensionless. The experiment described in section 5 involves processes occurring at Earth-like dimensions and thus the characteristic units differ from 1, the corresponding results are scaled back to dimensional units.

2.2. Numerical Method

2.2.1. Spatial Discretisation

[16] We solve equations (1) and (2) for the primitive variables v_i and p. The discrete solution of the two field formulation is defined by a grid based conservative finite difference scheme. The constraint imposed by incompressibility condition is effectively treated using the classical staggered grid arrangement of the primitive variables [*Harlow and Welch*, 1965]. In the staggered formulation used here, we solve for pressure which is defined at cell centers and for the component of velocity normal to the cell face Figure 1). The velocity component is located at the centroid of each cell face. For flow problems possessing a spatially variable viscosity, the viscosity is required to be defined at both the vertices, and the center of each control volume, in order for the discrete equations to conserve stress between neighboring control

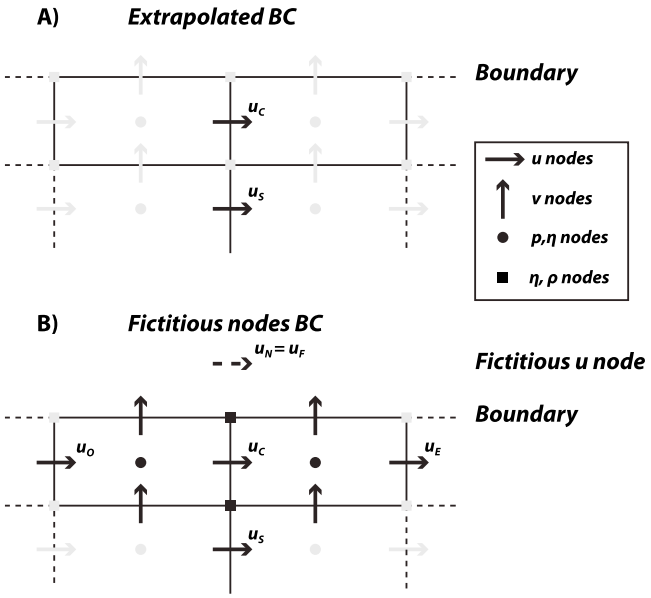

Figure 1. Spatial distribution of the primitive variables (u, v, p) and material properties (η, ρ) for a two-dimensional staggered grid and example of boundary conditions discretizations (case of the u momentum equation). The black symbols represent the nodes that are part of the stencil for the boundary equation discretization. The gray symbols represent the neighboring nodes that are not taken into account in the stencil. (a) The extrapolated boundary condition is formulated as a linear combination of two internal u nodes. (b) The fictitious node boundary condition implementation is achieved by discretizing the equations along the domain boundary. The dashed symbol represent the fictive point used for the formulation of this boundary equation.

volumes [*Patankar*, 1980]. This particular staggered grid difference scheme has been demonstrated to be robust in solving variable viscosity problems in mantle convection by numerous authors [*Ogawa et al.*, 1991; *Tackley*, 1993; *Ratcliff et al.*, 1995; *Harder and Hansen*, 2005; *Trompert and Hansen*, 1996; *Stemmer et al.*, 2006; *Tackley*, 2008] and in lithospheric dynamics [*Zaleski and Julien*, 1992; *Gerya and Yuen*, 2003, 2007; *Katz et al.*, 2007].

[17] The material properties viscosity and density are discretized in space via a set of markers, or particles. For a given property ϕ represented via the marker field, we adopt the following interpolant defined on the markers

$$\phi(\mathbf{x}) \approx \phi^m(\mathbf{x}) = \sum_{p=1}^{Nm} \delta(\mathbf{x} - \mathbf{x}_p)\phi_p^m, \tag{8}$$

where ϕ_p^m is the value of property ϕ (viscosity or density) defined at marker p, Nm is the number of markers, $\delta(\mathbf{x} - \mathbf{x}_p)$ denotes the standard Kronecker delta function and the marker coordinate is $\mathbf{x}_p$. For simplicity we express equation (8) via

$$\phi^m(\mathbf{x}) = \mathbf{Q}^T(\mathbf{x})\mathbf{\Phi}^m, \tag{9}$$

where $\mathbf{\Phi}^m$ is the vector of all marker values used to represent the field ϕ and $\mathbf{Q}^T$ is a row vector with each entry defining the Kronecker delta function for each marker p.

[18] To evaluate the finite difference stencil, we are required to interpolate the marker values for viscosity and density onto the relevant locations (cell vertex or centroid) within the FD grid. Here we derive the "marker-to-node" interpolation scheme defined by *Gerya and Yuen* [2003] by regarding the operation as an L_2 projection (least squares minimization) of the marker properties onto the vertices of a structured grid. To derive the interpolant in the study by *Gerya and Yuen* [2003], we first define grid based representation of the field ϕ. The grid is constructed from vertices of the cells defining each pressure control volume. Over each cell, the grid representation of field, which we denote by $\phi^g(\mathbf{x})$, is assumed to vary according to a bilinear function. Denoting the bilinear interpolant at node i by $N_i(\boldsymbol{x})$, we have the following approximation for ϕ over the grid

$$\begin{aligned}\phi(\mathbf{x}) \approx \phi^g(\mathbf{x}) &= \sum_{i=1}^{Nn} N_i(\mathbf{x})\phi_i^g \\ &= \mathbf{N}^T(\mathbf{x})\mathbf{\Phi}^g,\end{aligned} \tag{10}$$

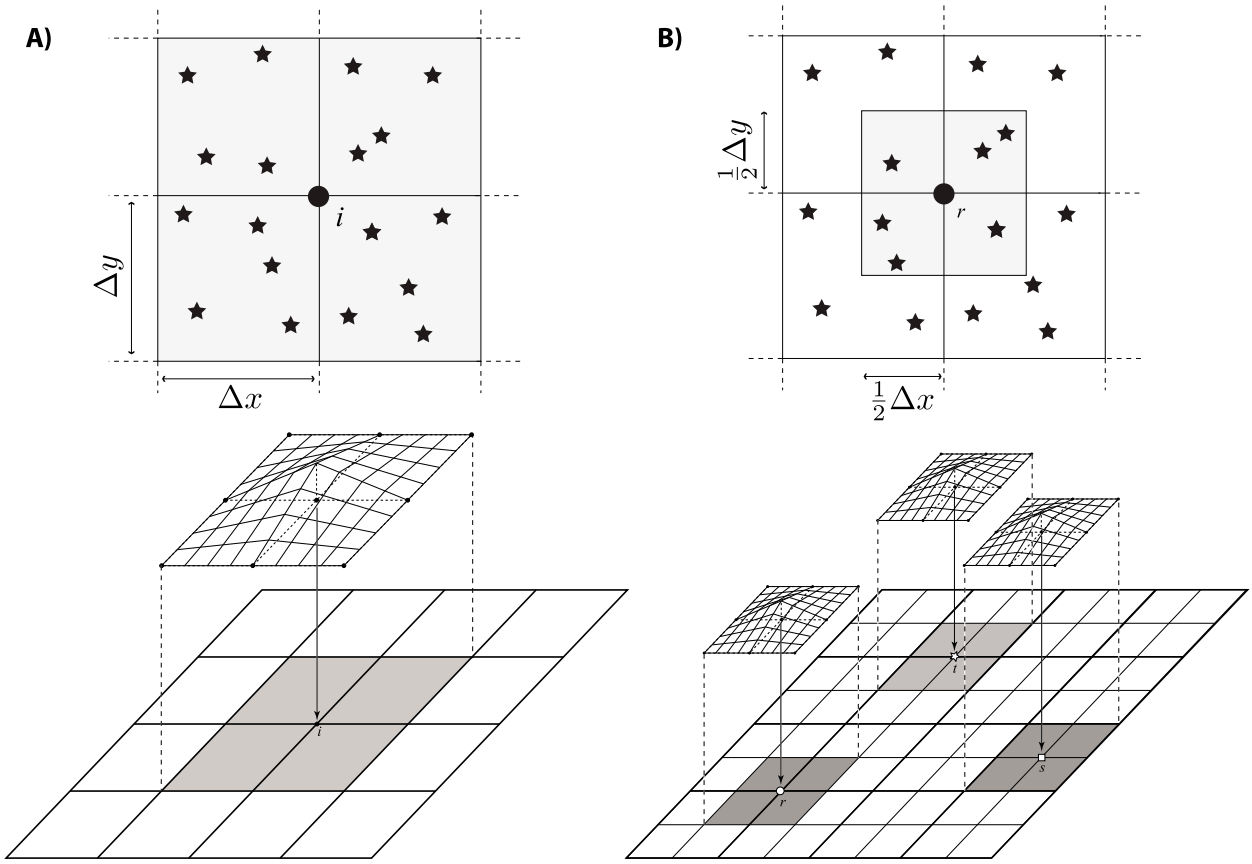

Figure 2. The "4-cell" and "1-cell" schemes for projecting properties defined on the markers (denoted by stars) onto a node (denoted by the solid circle). (a) The 4-cell scheme. The support of the interpolating function N_i associated with node i is indicated by the shaded region. Only markers within the support of node i contribute to the projection operation used to define the nodal value at i. The shape of the bilinear interpolation function for node i is indicated in the lower frame. (b) The 1-cell scheme. The thick lines in the lower frame indicate the grid used to discretize the Stokes equations, while the thin lines indicate the grid onto which marker properties are projected. The 1-cell scheme utilizes a compact support of size $\Delta x \times \Delta y$. The support for nodes r, s, t are indicated by the shaded regions. Only markers within the nodal support contribute to the projection operation for that node. The vertex and cell centered values on the grid used to discrete Stokes equations (points r and s, respectively) are directly obtained from the local projection scheme.

where Nn is the number of vertices in the mesh, $\mathbf{\Phi}^g$ is the vector of all nodal values used to represent the field ϕ and $\mathbf{N}^T$ is a row vector with each entry defining the interpolation function $N_i(\mathbf{x})$ for node i. The interpolating functions N_i have a compact support $\widehat{\Omega}$, implying the functions are only nonzero over a subset of the entire domain Ω. In this work, the compact support of each interpolant N_i, is $\widehat{\Omega} \equiv 2\Delta x \times 2\Delta y$, where Δx, Δy are the cell dimensions in the x and y direction, respectively. Furthermore, the grid interpolants N_i are a partition of unity, that is $\sum_{i=1}^{Nn} N_i(\mathbf{x}) = 1$. In Figure 2a we depict the compact support for a node i (denoted by the gray region) and the shape of the bilinear interpolation function N_i. Outside of the gray region, $N_i(\mathbf{x}) = 0$.

[19] The projection operator $\mathcal{P}$ can be defined as

$$\mathcal{P} : \phi^m(\mathbf{x}) \rightarrow \phi^g(\mathbf{x}).$$

Given that the number of markers and vertices in the mesh is not equal, a natural choice to define $\mathcal{P}$ is to use the L_2 projection of ϕ^m onto ϕ^g. The least squares minimization leads us to seek a solution of the following:

$$\min\left[\frac{1}{2}\int_{\Omega}(\phi^g(\mathbf{x}) - \phi^m(\mathbf{x}))^2 dV\right] = \min[J], \qquad (11)$$

where Ω is the model domain. Substituting equations (9) and (10) into equation (11) and computing $\partial J/\partial \mathbf{\Phi}^g = 0$ we obtain

$$\left(\int_\Omega \mathbf{N}(\mathbf{x})\mathbf{N}^T(\mathbf{x})dV\right)\mathbf{\Phi}^g = \int_\Omega \mathbf{N}(\mathbf{x})\mathbf{Q}^T(\mathbf{x})\mathbf{\Phi}^m dV, \quad (12)$$

and inserting equation (8) yields

$$\left(\int_\Omega \mathbf{N}(\mathbf{x})\mathbf{N}^T(\mathbf{x})dV\right)\mathbf{\Phi}^g = \sum_{p=1}^{N_m} \mathbf{N}(\mathbf{x}_p)\phi_p^m. \quad (13)$$

[20] The "marker-to-node" interpolation of *Gerya and Yuen* [2003] is obtained from equation (13) by making the following approximations; (1) replacing the matrix on the left hand side by a diagonal matrix defined by summing the entries in each row, i.e.,

$$\begin{aligned} N_i(\mathbf{x})N_j(\mathbf{x}) &\approx N_i(\mathbf{x})\left(\sum_{k=1}^{Nn} N_k(\mathbf{x})\right)\delta_{ij} \\ &= N_i(\mathbf{x})\delta_{ij}, \end{aligned} \quad (14)$$

where the summation in brackets was eliminated since N_i form a partition of unity and (2) evaluating the integrals using a numerical quadrature defined by the markers within the compact support of each N_i. Approximating $\mathbf{NN}^T$ by a diagonal matrix makes the projection operation completely local to each node i in the mesh. This choice is predominately made to reduce the computational cost by eliminating the need to solve a matrix problem. Nevertheless, it is usually more desirable to utilize a local L_2 approximation, as global L_2 tend to produce overly smooth fields. Given that the interpolant used for the marker fields are Kronecker delta functions (see equation (9)), the most natural quadrature scheme to use is a Monte Carlo method in which the markers coordinates define the abscissa of the quadrature scheme and every quadrature point is assigned the same quadrature weight, with the only constraint that the sum of the weights should equal the volume of the integration domain. Incorporating the above two assumptions, and invoking equation (9) reduces equation (12) to the following:

$$\phi_i^g = \frac{\sum_{p=1}^{N_m} N_i(\mathbf{x}_p)\phi_p^m}{\sum_{p=1}^{N_m} N_i(\mathbf{x}_p)}. \quad (15)$$

[21] We note that the L_2 interpolant defined in equation (12) was $O(h^2)$ accurate, where h represents the grid spacing, as the function space onto which we projected the marker field was bilinear. However, the approximated interpolant in equation (15) possesses a reduced rate due to the choice of quadrature scheme utilized. In the worst case, classical Monte Carlo quadrature with random abscissa converges like $O(n^{-1/2})$, where n is the number of points, while quasi Monte Carlo methods using pseudo random abscissa can converge as fast as $O(\sqrt{\log(n)}/n)$. The abscissa used in our quadrature scheme are determined via the coordinates of the markers, which are inherently nondeterministic and are the result of the solution to Stokes flow. Consequently, we anticipate that the quadrature rule employed here will tend toward the classical Monte Carlo limit and thus the expected order is $O(\overline{H}^{1/2})$, where $\overline{H}$ is the average spacing of the markers. In this work, the projection depicted in Figure 2a will be referred to as the "4-cell" scheme.

[22] In the study by *Gerya and Yuen* [2007], a "local" variant of the projection operator in equation (12) was proposed. This local marker-to-node projection is depicted in Figure 2b. The principal difference is that the marker properties are projected onto a grid of finer resolution (thin lines, bottom frame) than the grid used to discretize Stokes equations (thick lines, bottom frame), thus the compact support of each interpolant N_i is now $\widehat{\Omega} \equiv \Delta x \times \Delta y$. While developed heuristically, numerical experiments revealed that this local projection method yielded more accurate results [*Gerya and Yuen*, 2007]. Given that we have shown that the interpolant used by Gerya and coworkers is an approximate L_2 projection, it is apparent why the local variant yields more accurate results. Specifically, we note that while the order of the local L_2 projection is the same variant depicted in Figure 2a, the discretization parameter h has been reduced by a factor of two, which thus also reduces the error. In the local projection scheme, vertex values and cell center values (denoted by r and s, respectively, in Figure 2b) are obtained from application of equation (15) on the finer grid. Note that the midside values (denoted by t) are not required by the finite difference stencil. The projection depicted in Figure 2b will be referred to as the "1-cell" scheme.

2.2.2. Temporal Discretisation

[23] The Lagrangian markers are used to discretize each composition field C. In the Lagrangian frame

of reference, the solution of equation (7) can be obtained by solving the following two equations:

$$\frac{DC_p}{Dt} = 0, \qquad \frac{d\mathbf{x}_p}{dt} = \mathbf{v}_p, \tag{16}$$

where C_p, $\mathbf{x}_p$, $\mathbf{v}_p$ are the composition, coordinate and velocity vector of marker p, respectively. The solution of $DC_p/Dt = 0$ is trivially obtained with the marker representation. The kinematic equation is solved using a fourth-order Runge-Kutta (RK4) time stepping scheme applied to each marker p. We do not reevaluate the flow field during the application of RK4, thus the method is fourth-order accurate in space only. The velocity field at the marker $\mathbf{v}_p$, is obtained by interpolating the flow field computed on the finite difference grid to the marker coordinate $\mathbf{x}_p$. After the markers have been advected, the material properties are interpolated from the new marker positions to the Eulerian grid using either the 4-cell or 1-cell projection defined by equation (15). Alternatively, higher-order time integrators such as the predictor-corrector method are employed in the community [*Weinberg and Schmeling*, 1992; *Schmeling et al.*, 2008], this method achieves second-order (in time) accuracy but requires to solve the discrete Stokes equations twice per time integration.

2.2.3. Boundary Condition Implementation

[24] We have used two different techniques to impose boundary conditions (BC) on the non–boundary matching nodes of the staggered grid. The first method (extrapolated boundary condition) enables to describe the stress or velocity value at the boundary by setting a condition on two nodes inside the domain (extrapolation). A linear combination of the velocities at those two nodes defines a velocity gradient, the value of the velocity at the boundary is therefore set by the value of the gradient. For instance the u component of a free slip boundary condition at the top of the domain (assuming zero normal velocity) is expressed as

$$\left.\frac{\partial u}{\partial y}\right|_{\text{top}} = 0 \Longrightarrow u_C - u_S = 0, \tag{17}$$

where the node labeling is depicted in Figure 1. For the no slip case, we extrapolate to the boundary, thus

$$u|_{\text{top}} = 0 \Longrightarrow u_C - \frac{1}{3}u_S = 0. \tag{18}$$

[25] The stencil corresponding to this boundary equation only contains two points and additional constraints are needed while solving for pressure. This condition is usually fulfilled by setting additional pressure constrain such as zero horizontal pressure flux in the corners of the domain [*Gerya*, 2010]. Given the fact that the boundary condition is defined via extrapolation, we expect this implementation to be first order in space. A second method (fictitious node method) is derived by discretizing the momentum equations along the domain boundaries. The usual stencil is modified to account for "virtual nodes" outside of the domain. These virtual nodes are used to define the velocity flux at the boundary of the domain, they are not explicitly included into the system of equations. The isoviscous u momentum equation stencil at the top of the domain is written as

$$\frac{\partial \sigma_{xx}}{\partial x} + \eta\left(\frac{u_F + u_S - 2u_C}{\Delta y^2}\right) + \eta\frac{\partial^2 v}{\partial y \partial x} - \frac{\partial p}{\partial x} = -\rho g_x, \tag{19}$$

with

$$u_F = u_C, \tag{20}$$

for a free slip case and

$$u_F = -u_C, \tag{21}$$

for a no slip case.

[26] This method do not require any additional pressure constrains, thus no boundary conditions are required while solving for pressure. With this discretization of the boundary condition, each partial derivative is approximated by means of central finite differences and we therefore expect this method to be second-order accurate in space.

2.2.4. Free Surface Treatment

[27] As shown by *Kaus et al.* [2010], the introduction of a free surface boundary condition in geodynamic simulations can induce artificial numerical oscillations in the free surface. This phenomena was coined the "drunken seaman" instability. The free surface in these models represents an interface between air and rock, and this is characterized by a sharp jump in density (~10^3 kg.m^{-3}). A large displacement of this interface within a single time step can therefore give rise to severe "out-of-balanceness" [*Kaus et al.*, 2010]. Physically, this imbalance may occur when the employed time step exceeds the isostatic relaxation time [*Fuchs et al.*, 2011]. Such a situation is likely to occur when an explicit advection scheme is used, since the nonlinear residual associated with the advected coordinates (at time $t + \Delta t$), and the evaluation of the force term and stresses (at time t) is not

guaranteed to be small. The "drunken seaman" instability can occur when the free surface is explicitly tracked, such as in a body fitted Lagrangian finite element method, or when the free surface boundary condition is approximated via the "sticky air" approach [*Schmeling et al.*, 2008], which is commonly used in Eulerian-Lagrangian finite difference methods in which explicit meshing of the interface is not possible. Several methods can be used to stabilize the evolution of the free surface, which either involve solving the nonlinearity related to advection or introducing higher-order terms arising from a Taylor series expansion of the momentum balance equation. Here we focus on the second approach applied to our staggered grid finite difference discretization.

[28] *Kaus et al.* [2010] showed that a higher-order Taylor series expansion of the weak formulation of the momentum balance equation leads to an expression of a correction term which has the form of a boundary traction. This correction term is then discretized and added to the original Stokes stiffness matrix. Following this methodology, we derive a similar correction term for the strong form of the Stokes equations (such as used with the finite difference method) by performing a Taylor series expansion of equation (1) about the point $\mathbf{x} + \theta\Delta t\mathbf{v}$, where Δt is the time step and $0 < \theta < 1$ is an arbitrary parameter used to limit the size of the displacement increment. The expansion of the stress tensor σ_{ij}, is given by

$$\sigma_{ij}(\mathbf{x} + \theta\Delta t\mathbf{v}) \approx \sigma_{ij}(\mathbf{x}) + \theta\Delta t\ v_k \left[\sigma_{ij}(\mathbf{x})\right]_{,k} + O(\Delta t^2), \quad (22)$$

where the subscript , k denotes a partial derivative with respect to x_k. The gradient of the stress tensor $\sigma_{ij,j}$, is then

$$\sigma_{ij,j}(\mathbf{x} + \theta\Delta t\mathbf{v}) \approx \sigma_{ij,j}(\mathbf{x}) + \theta\Delta t\ v_k \left[\sigma_{ij}(\mathbf{x})\right]_{,jk} + \theta\Delta t\ v_{k,j} \left[\sigma_{ij}(\mathbf{x})\right]_{,k} + O(\Delta t^2). \quad (23)$$

Assuming that $\mathbf{g}$ is constant, we expand the density as

$$\rho(\mathbf{x} + \theta\Delta t\mathbf{v}) \approx \rho(\mathbf{x}) + \theta\Delta t\ v_k [\rho(\mathbf{x})]_{,k} + O(\Delta t^2). \quad (24)$$

Inserting equations (23) and (24) into equation (1) and keeping only the terms which are linear in v_k and those of $O(\Delta t)$, we obtain the perturbed momentum balance equation

$$\sigma_{ij,j}(\mathbf{x}) + \theta\Delta t\ \rho(\mathbf{x})_{,k} v_k\ g_i = -\rho(\mathbf{x}) g_i. \quad (25)$$

Here, the term $\theta\Delta t\ \rho(\mathbf{x})_{,k}\ v_k$ represents a higher-order correction which is a function of the velocity field, v_k. We denote the discrete representation of the momentum equation in equation (25) via

$$\mathbf{Ku} + \mathbf{Lu} + \mathbf{Gp} = \mathbf{f}, \quad (26)$$

where $\mathbf{Ku}$ is discrete gradient of the stress tensor, $\mathbf{Gp}$ is the discrete pressure gradient, $\mathbf{f}$ is the discrete body force and $\mathbf{Lu}$ is the stabilization term. The construction of $\mathbf{L}$ requires the current time step Δt and the evaluation of the density gradient at each of the u, v nodes. In our FD-MIC formulation, this is achieved by central finite differences. We evaluate $\frac{\partial\rho}{\partial x} \approx \frac{\Delta\rho}{\Delta x}$ and $\frac{\partial\rho}{\partial y} \approx \frac{\Delta\rho}{\Delta y}$ at the u and v nodes, respectively. The first-order derivatives are computed using values of density defined at the cell center (i.e., at the pressure node). The density at the cell center is interpolated from the marker density field, or averaged from a density field defined on the vertices of the grid.

3. Discretization Errors and Convergence

3.1. Errors in Approximate Solutions of PDEs

[29] Errors in the approximate solution of partial differential equations (PDEs) arise from four main sources.

[30] 1. The discretization error (or truncation error), which is defined as the difference between a given mathematical model (analytic solution) and its discretized expression. In the case of the finite difference method, the derivative of a function is numerically estimated by first assuming that the function is continuous, and then by replacing the continuous derivative with a truncated Taylor series about a point. The discretization error is therefore generated by the truncation of the Taylor expansion and is proportional to the remainder ($O(h^n)$). This type of discretization error is termed a locally generated error by *Roy* [2010].

[31] 2. An additional discretization error may occur in the definition of the coefficients within the PDE. Coefficients may consist of terms on the right side of the equation (e.g., density), or terms within the differential operator itself (e.g., viscosity). Coefficients will possess a discretization error if they are obtained by interpolation (e.g., projection of markers properties to nodes), or if they are a function of variables which were discretized. Typical examples of the latter include temperature or strain rate–dependent viscosity where temperature (or velocity) are discretized over a grid, and the viscosity is

required at a location which doesn't coincide with a discretization point in the grid.

[32] 3. Roundoff errors arising from the numerical representation of real, continuous numbers, with a finite precision representation. This error therefore depends on the precision (number of digits) which is employed to represent floating point numbers in a numerical scheme.

[33] 4. The error resulting from the solution of systems of linear equations.
The use of direct solvers (such as LU, Cholesky decomposition) can minimize this type error, at least to the extent possible with finite precision arithmetic (see item 3 above). However, if iterative methods are used, the error induced is a result of stopping condition used to terminate the iterative cycle. Robust stopping conditions should monitor the residual associated with the system and the current estimate of the solution. However, one still needs to specify a measure of when the residual is "small enough" to conclude that the iterative method has converged.

[34] We here focus on the evaluation of the discretization error of the FD-MIC scheme. Our specific interest is to determine the convergence of the method in the case where viscosity jumps (discontinuous coefficients) occur at a subgrid level. The discretization error of the FD-MIC scheme can be seen as the combination of the truncation error of the staggered grid (including boundary condition discretization) and the error related to the projection of material properties onto the nodes. In this study, the discrete system of equations describing Stokes flow was solved using a direct factorization technique, thus eliminating any error associated with using an iterative method. All calculations were performed using double precision arithmetic.

3.2. Measuring Convergence of the Discretization: Methodology

[35] Several methods are available in order to study the discretization error of numerical schemes [*Roache*, 1997; *Roy*, 2010]. We here focus on measuring the order of convergence of the primitive variables of our discrete Stokes problem. To do so, we employed two-dimensional analytic solutions which can be utilized to determine the exact velocity and pressure values at each node of our grids. In order to compute the discretization error, we utilize the L_1 norm, which for a scalar quantity ϕ, is defined as follows:

$$\|\phi\|_1 = \int_\Omega |\phi| dV, \tag{27}$$

where Ω is the model domain. For a vector quantity $\mathbf{w} = (s, t)$ we have

$$\|\mathbf{w}\|_1 = \|s\|_1 + \|t\|_1 = \int_\Omega (|s| + |t|) dV. \tag{28}$$

We define the pressure error as

$$\|e_p\|_1 := \|p - p_{\text{exact}}\|_1, \tag{29}$$

where p_{exact} is the exact value of the pressure. The L_1 error for the velocity $\mathbf{u} = (u, v)$, is defined via

$$\|e_{\mathbf{u}}\|_1 := \|e_u\|_1 + \|e_v\|_1 = \|u - u_{\text{exact}}\|_1 + \|v - v_{\text{exact}}\|_1, \tag{30}$$

where u_{exact} and v_{exact} are the exact values of the u, v velocity components. For numerical computations we approximate the above integrals via a one point quadrature rule, i.e.,

$$\|\phi\|_1 \approx \|\phi\|_1^h := \sum_e |\phi(\mathbf{x}_e)| \, V_e, \tag{31}$$

where V_e is the representative volume for the point $\mathbf{x}_e$. For FD schemes, the appropriate volume to use in equation (31) is the control volume associated with each node. Within staggered grid FD schemes, the control volume associated with the p and u, v degrees of freedom are different. In our results, we utilize two-dimensional meshes containing $M \times M$ elements. As a result, we have $(M+1) \times M$ nodes for u, $M \times (M+1)$ nodes for v, and $M \times M$ nodes for pressure. From this, we define the following discrete L_1 norm for pressure as

$$\|p\|_1 \approx \sum_{I=1}^{M} \sum_{J=1}^{M} |p_{I,J}| \Delta x \Delta y, \tag{32}$$

where $\Delta x \Delta y$ is the cell volume For the velocity components we have

$$\|u\|_1 \approx \frac{1}{2} \sum_{J=1}^{M} |u_{1,J}| \Delta x \Delta y + \sum_{I=2}^{M} \sum_{J=1}^{M} |u_{I,J}| \Delta x \Delta y + \frac{1}{2} \sum_{J=1}^{M} |u_{(M+1),J}| \Delta x \Delta y, \tag{33}$$

$$\|v\|_1 \approx \frac{1}{2} \sum_{I=1}^{M} |v_{I,1}| \Delta x \Delta y + \sum_{I=1}^{M} \sum_{J=2}^{M} |v_{I,J}| \Delta x \Delta y + \frac{1}{2} \sum_{I=1}^{M} |v_{I,(M+1)}| \Delta x \Delta y. \tag{34}$$

[36] The order of convergence of the discretization is determined by computing the numerical solution defined on a sequence of uniformly refined grids,

and computing the L_1 norm of $e_{\mathbf{u}}$ and e_p on each grid. Following this, a least squares regression is performed on the log10 of the error norm and the cell size h. We relate the convergence rate of the L_1 norms for velocity and pressure errors to the order of convergence via

$$\|e_{\mathbf{u}}\|_1 \leq Ch^{r_u}, \qquad \|e_p\|_1 \leq Ch^{r_p}, \tag{35}$$

where h is the mesh size, C is a constant independent of the grid resolution h, and r_u, r_p are the order of convergence for velocity and pressure fields, respectively. In all our experiments, the grid possesses the same number of vertices N in each direction. We define our grid sequence using $N = \{41, 81, 101, 201, 301, 401, 501, 601, 701, 801, 901, 1001\}$.

4. Numerical Experiments

4.1. Idealized Models Used in the Convergence Study

[37] To study the error distributions and convergence properties of our numerical scheme, we carried out two sets of experiments. Each of these tests is aimed at studying the effect of a spatially variable coefficient (viscosity) on the discretization. We define a global measure of the viscosity contrast over the entire domain Ω via $\eta^* = \max(\eta(\mathbf{x}))/\min(\eta(\mathbf{x}))$. The first test focuses on the buoyancy-driven flow in a box containing a one-dimensional viscosity structure. The second test addresses the influence of a large but smooth variation of viscosity within a box where the flow is driven by buoyancy. The third test investigates a pure shear deformation field, which is perturbed by the presence of a two-dimensional, circular, highly viscous inclusion.

4.1.1. One-Dimensional Viscosity Structure: SolCx

[38] The first series of convergence test were performed using a two-dimensional analytical solution of a variable viscous Stokes flow problem which we identify as SolCx. The model domain is defined as $\Omega \equiv [0, 1] \times [0, 1]$. The boundary conditions on all sides of the domain are prescribed to be free slip, implying that the normal velocity to each wall is zero, and the tangential stress along the wall vanishes. Internal to the domain, fluid flow is driven by a sinusoidal force given by

$$\mathbf{F} = (0, -\sin(\pi y)\cos(\pi x))^T. \tag{36}$$

In practice this force is imposed by setting a constant gravity acceleration (x component equal to 0 and y component equal to 1) and the allowing the density field to vary in space according to

$$\rho(x, y) = \sin(\pi y)\cos(\pi x). \tag{37}$$

Experiments were carried out for both isoviscous and variable viscosity case, in the latter case the viscosity field is discontinuous and is given by

$$\eta(x, y) = \begin{cases} 1, & \text{if } 0 \leq x \leq 0.5 \\ 10^6, & \text{if } 0.5 < x \leq 1. \end{cases} \tag{38}$$

This setup allows for sharp viscosity jumps of large magnitude which is a typical requirement for geodynamic applications (see Figure 3). Furthermore, the discontinuous viscosity structure provides a more challenging test of both the discretization and the solver in comparison to solutions with continuous viscosity structures. A complete description of the analytic solution is provided by *Zhong* [1996]. The source code used in our study to evaluate the analytic solution is available from the open source package Underworld [*Moresi et al.*, 2007]. Since the flow is driven by the density gradients, we will again use this test to analyze the influence of the free surface stabilization scheme on the convergence of the FD-MAC method.

4.1.2. Smooth Viscosity Variation in One Dimension: SolKz

[39] In order to investigate the effect of a large and smooth viscosity variation on our discretization, we utilized the analytic solution from *Revenaugh and Parsons* [1987], which here we have termed SolKz. This solution allows for a exponential variation of viscosity from the bottom to the top of the model domain which is defined as $\Omega \equiv [0, 1] \times [0, 1]$. All the boundaries are free slip and the flow is driven by a smooth density distribution, the forcing term is expressed as

$$\mathbf{F} = (0, -\sin(2y)\cos(3\pi x))^T. \tag{39}$$

and the viscosity increases from the bottom to the top of the box according to

$$\eta(y) = \exp(2By) \tag{40}$$

with the parameter B controlling the magnitude of the overall viscosity variation. Here we choose B such that over the vertical extend of the domain we have viscosity contrast of $\Delta\eta^* = 10^6$. The density,

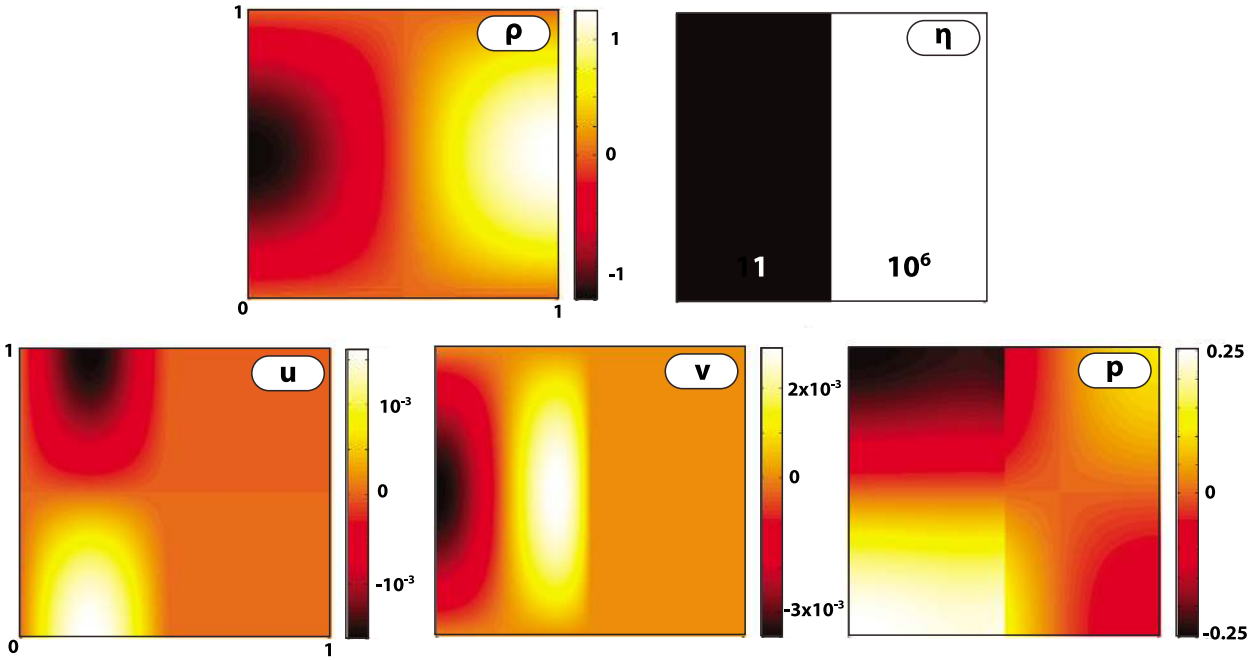

Figure 3. Material properties and the analytic solution for SolCx. The ρ and η are the density and viscosity distributions, u, v are the analytic x, y components of velocity, respectively, and p is the analytic pressure field. The vertical component of gravity acceleration is 1.

viscosity distribution and the resulting flow field are depicted in Figure 4. Similarly to the SolCx test, the source code used to evaluate the analytical solution is part of the open source package Underworld.

4.1.3. Two-Dimensional Viscosity Structure: Pure Shear Inclusion Test

[40] The third series of convergence test were carried out using the analytical solution for an inclusion in a

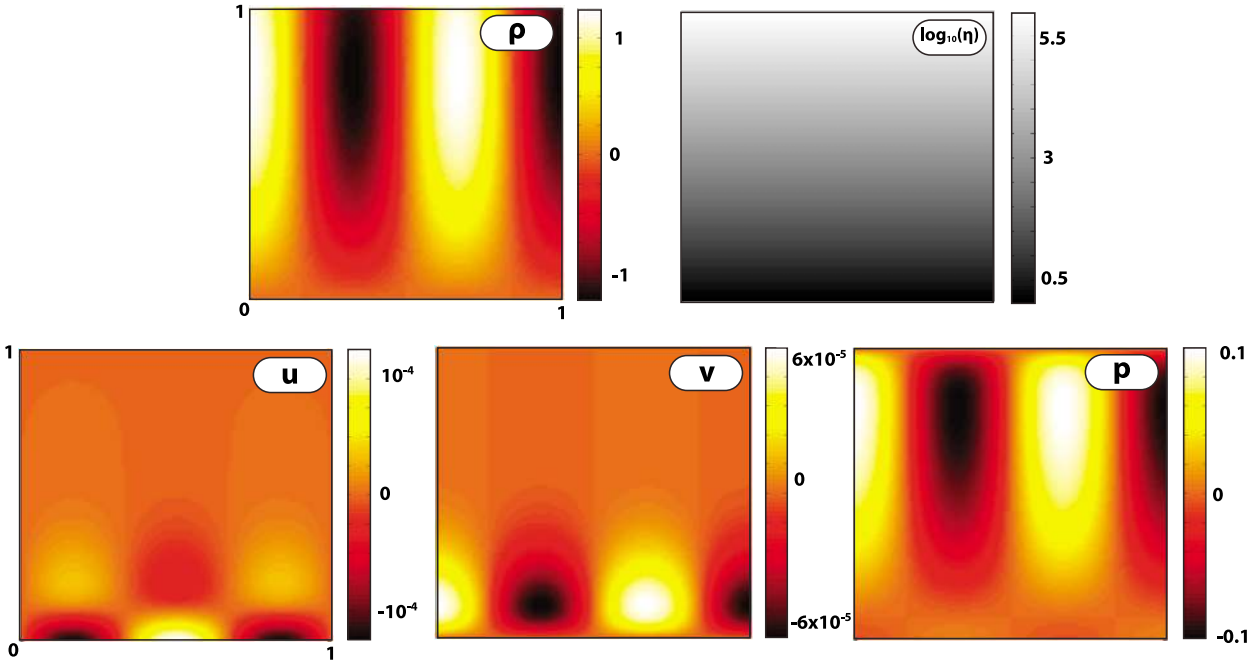

Figure 4. Density (ρ), viscosity (η), and flow pattern (u, v, p) for the analytic solution SolKz.

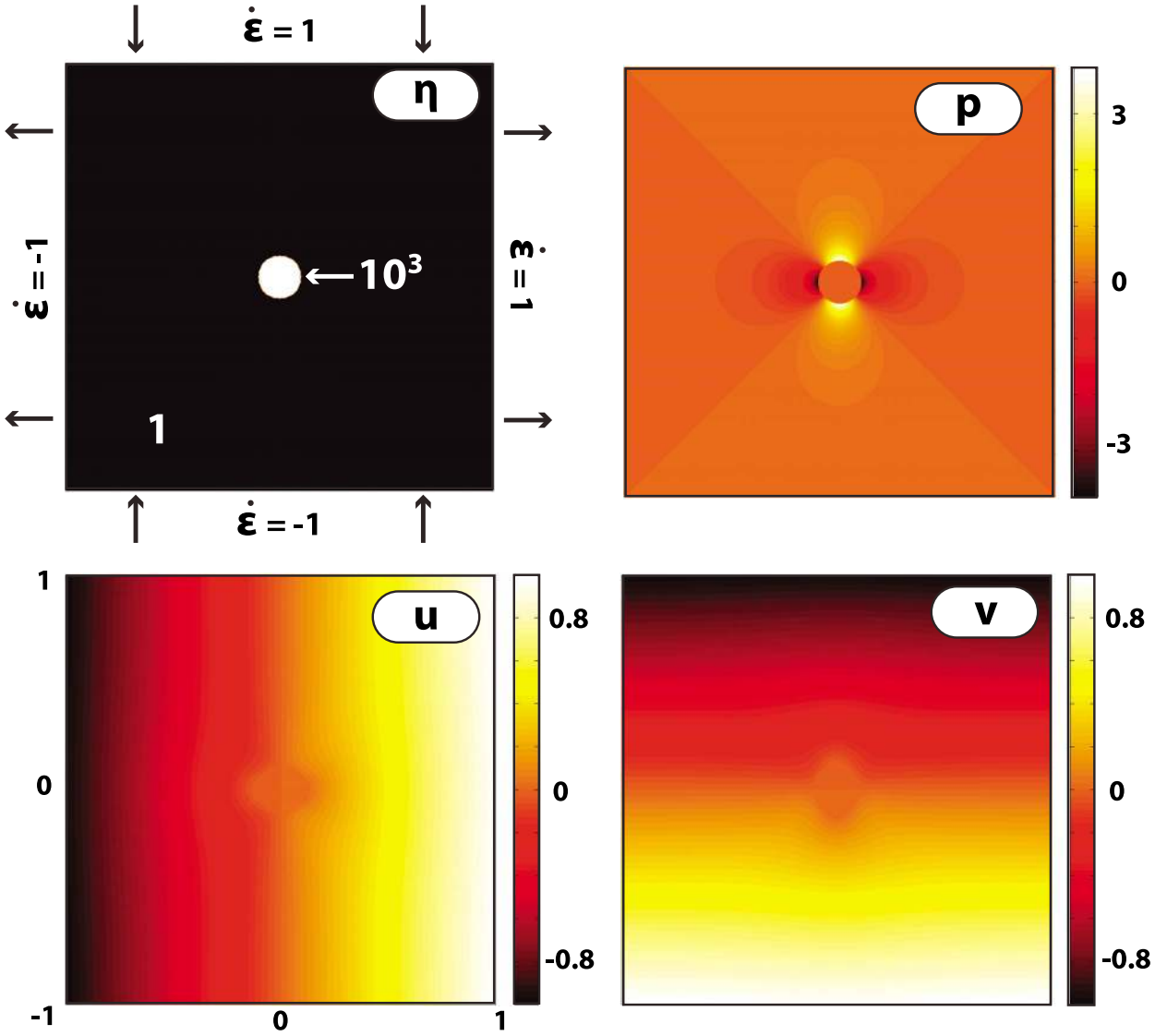

Figure 5. Viscosity structure (η) and analytic solution for velocity (u, v) and pressure (p), for the pure shear inclusion test [*Schmid and Podladchikov*, 2003]. For this setup, the flow is driven by a strain rate boundary condition ($\dot{\epsilon} = 1$), and the buoyancy forcing term is 0 (e.g., $\rho = 0$ or $g_y = 0$).

weak matrix undergoing pure shear. The derivation as well as the scripts that can be used to compute the analytic are available in the study by *Schmid* [2002] and *Schmid and Podladchikov* [2003]. For this problem, the model domain is defined as $\Omega \equiv [-1, 1] \times [-1, 1]$ and contains a circular shaped inclusion at the origin. The inclusion has a radius, R_{inc} of 10% the length of the domain. The viscosity field is given by

$$\eta(x,y) = \begin{cases} 1, & \text{if } x^2 + y^2 > {R_{inc}}^2 \\ 10^3, & \text{if } x^2 + y^2 \leq {R_{inc}}^2, \end{cases} \quad (41)$$

as used by *Deubelbeiss and Kaus* [2008]. The flow is driven by a pure shear strain rate boundary condition and the force vector, ρg_i is zero (Figure 5). In this test, the circular shape of the inclusion ensures that the viscosity jump is never aligned with cartesian coordinate system, and thus is never aligned via the finite difference stencil. Consequently, this test is particularly relevant since bodies of arbitrary shape (e.g., plumes, slabs) typically develop during the evolution of geodynamic simulations.

4.2. Staggered Grid Discretization

[41] In the first set of experiments, we used the analytical solution SolCx to examine the convergence properties of the staggered grid finite difference

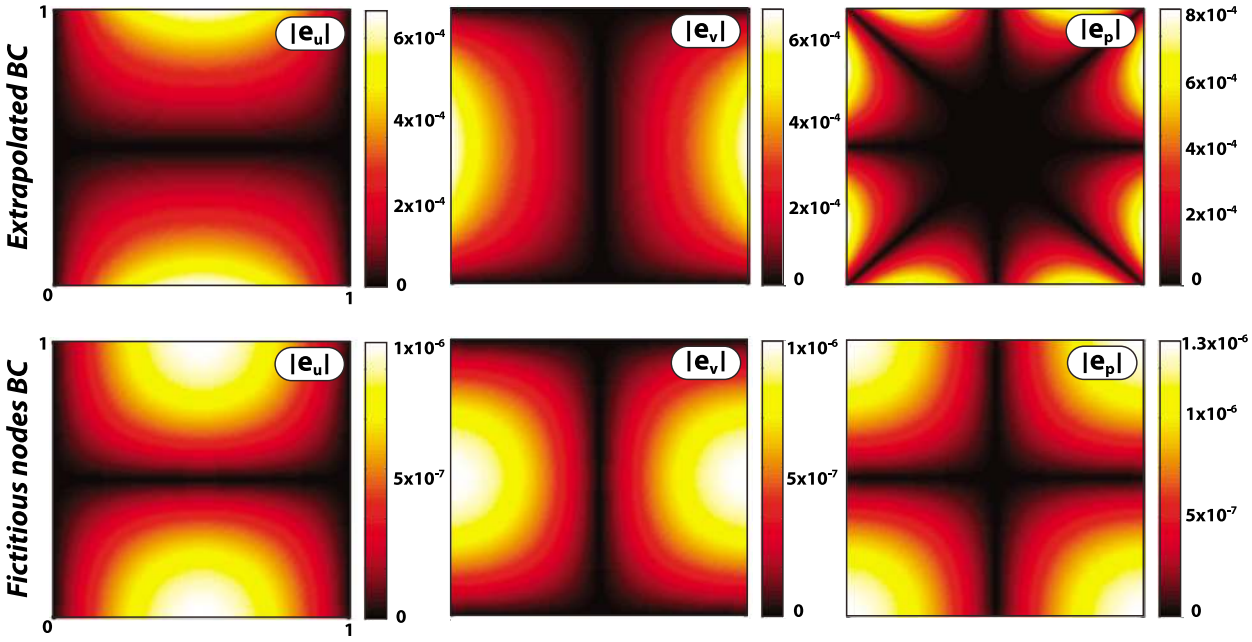

Figure 6. Spatial distribution of the absolute value of the discretization error (e_u, e_v, e_p) for the variables u, v, and p. Comparison between extrapolated and fictitious node boundary condition implementations. Maximum errors are located at the domain boundaries. The error pattern and magnitudes between the two methods are notably different. The test was carried out using the isoviscous SolCx setup with a grid resolution of 101 × 101 nodes.

discretization These experiments do not employ markers to represent the material properties η, ρ. The finite difference stencil was thus defined by directly evaluating equations (36) and (38). Experiments were performed using the two different boundary condition implementations described in section 2.2.3.

4.2.1. SolCx: Isoviscous

[42] Here we consider a spatially constant viscosity field, i.e., $\eta(x, y) = 1$. These tests were performed in order to measure convergence of the method for an optimal case, and to assess the error associated with the different boundary condition implementations. In Figure 6, the error distribution for a 101 × 101 grid resolution is shown. A clear influence of the type of boundary condition can be observed. With both implementations, the maximum error for all fields is confined along the boundary of the domain. However, the error obtained using the extrapolated BC approach is significantly larger. At this resolution, we observe that the velocity and pressure errors are approximately 2 orders of magnitude smaller when the fictitious node BC implementation is used. The L_1 errors for a sequence of grid resolutions is shown in Figure 7a, and the computed rates are provided in Table 1. As we expected, the velocity and pressure obtained using extrapolated BC discretization converge to the analytical solution with a rate of ~1. The fictitious node boundary condition implementation yields **u**, p fields which both converge at a rate of ~2. From Figure 7a, it is apparent that the absolute value of the velocity and pressure errors in L_1 are much lower (for all grid resolutions) when the fictitious node BC is used. Given these results, we will refer to extrapolated BC method and the fictitious node BC implementation as the "first-order" and "second-order" BC methods in the following sections.

4.2.2. SolCx: 10^6 Viscosity Jump

[43] In this second test, a large discontinuous jump in viscosity (10^6 Pa.s) was introduced. The discretization error for a 101 × 101 grid resolution is shown Figure 8. In comparison with the isoviscous results (Figure 6), the location of the maximum error is no longer only confined along the boundary of the domain. Rather, we now observe that maximum errors in u, v occur within the low-viscosity region, and share a similar spatial correlation with the isoviscous case if we consider only the low-viscosity domain ($x < \frac{1}{2}$). For the v velocity component, the maximum absolute error is located at the jump, with a magnitude of $|e_v| \approx 10^{-4}$ for both

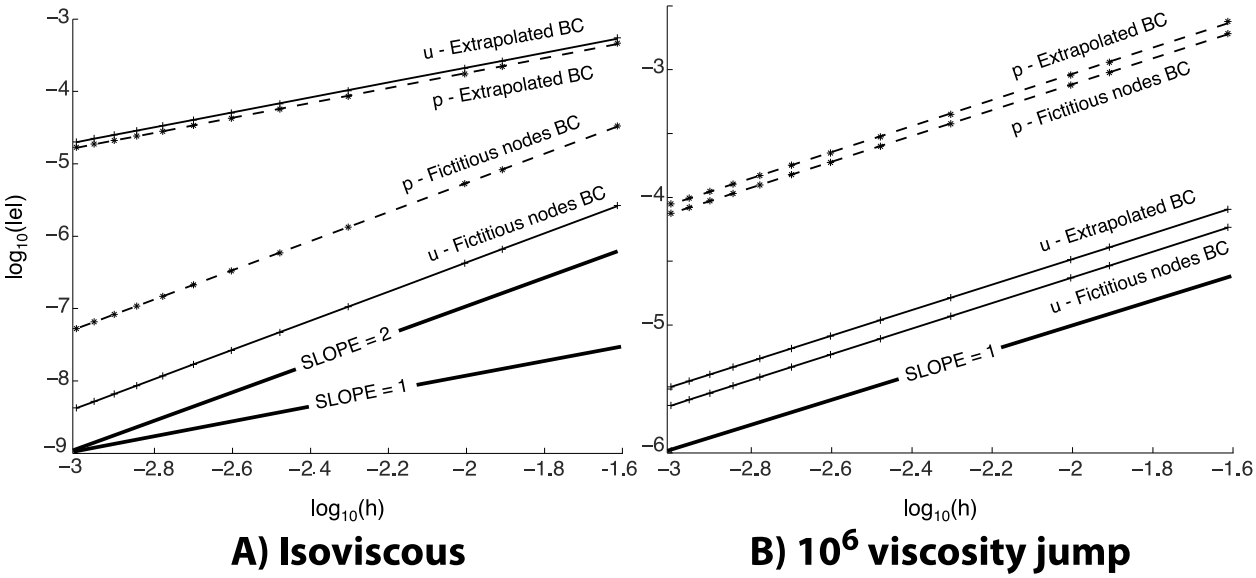

Figure 7. Velocity and pressure L_1 error norms with increasing resolution for the SolCx test. Viscosity and density are directly sampled, and therefore no interpolation is used. (a) First-order convergence is achieved while using extrapolated boundary conditions. Second-order convergence is obtained with fictitious node boundary conditions. (b) As soon as a jump in viscosity is introduced, both extrapolated and fictitious node boundary conditions converge at a first-order rate.

boundary condition implementations. The effect of the BC implementation remains visible for both u and v, at the boundaries second-order BC produces errors which are approximately 1 order of magnitude smaller than for the first-order case. Pressure errors are distributed at the jump and close to the boundaries. In contrast with the isoviscous case, the pressure errors are much larger than the velocity errors (≈10–100 times) and significantly larger (≈100–1000 times) than in the isoviscous case. The discontinuous variation of the viscosity not only has a strong influence on the spatial distribution of errors, but also on the order of convergence of the computed velocity and pressure fields. The L_1 errors for the variable viscosity case are shown in Figure 7b, and the computed rates are provided in Table 1. The most noticeable feature is that the choice of boundary condition implementation is much less critical. This is apparent as we observe that the convergence of the velocity and pressure errors in L_1, for both boundary condition implementations, are approximately first order. The magnitudes of the L_1 error for velocity and pressure error are lower when using second-order boundary conditions, however the difference is less than 0.25 of an order of magnitude. For this particular test, we observed different results if an even grid sequence was employed. The even grid sequence corresponds to a situation where the central pressures nodes are located directly on the viscosity jump. Using an even grid sequence with second-order boundary conditions lead to an improvement of the velocity and pressure errors in L_1, with orders of convergence of $r_u = 2.0$ and $r_p = 1.0$, respectively. Due to the super convergent nature of these rates, we regard meshes with viscosity jumps aligned with pressure nodes as a special case. While it is of interest to understand the reason for the apparent super convergent behavior, in practice we rarely ever encounter material property contrast which can be aligned with the grid, thus we do not study this special case any further here.

4.3. Staggered Grid and Marker-in-Cell Discretization

[44] In the second set of experiments, we defined the material properties (η, ρ) via markers, therefore both viscosity and density fields were projected

Table 1. Order of Convergence of the L_1 Error Norm Between Analytics and Numerics Without Using Interpolation[a]

	BC (First Order)		BC (Second Order)	
	η^* (1)	η^* (10^6)	η^* (1)	η^* (10^6)
r_u	1.0648	1.0052	2.0276	1.0064
r_p	1.0416	1.0026	2.0297	1.0114

[a]Results are produced using the analytical solution SolCx. Comparison between two boundary condition implementations. Results are calculated for two different fluid viscosity contrasts.

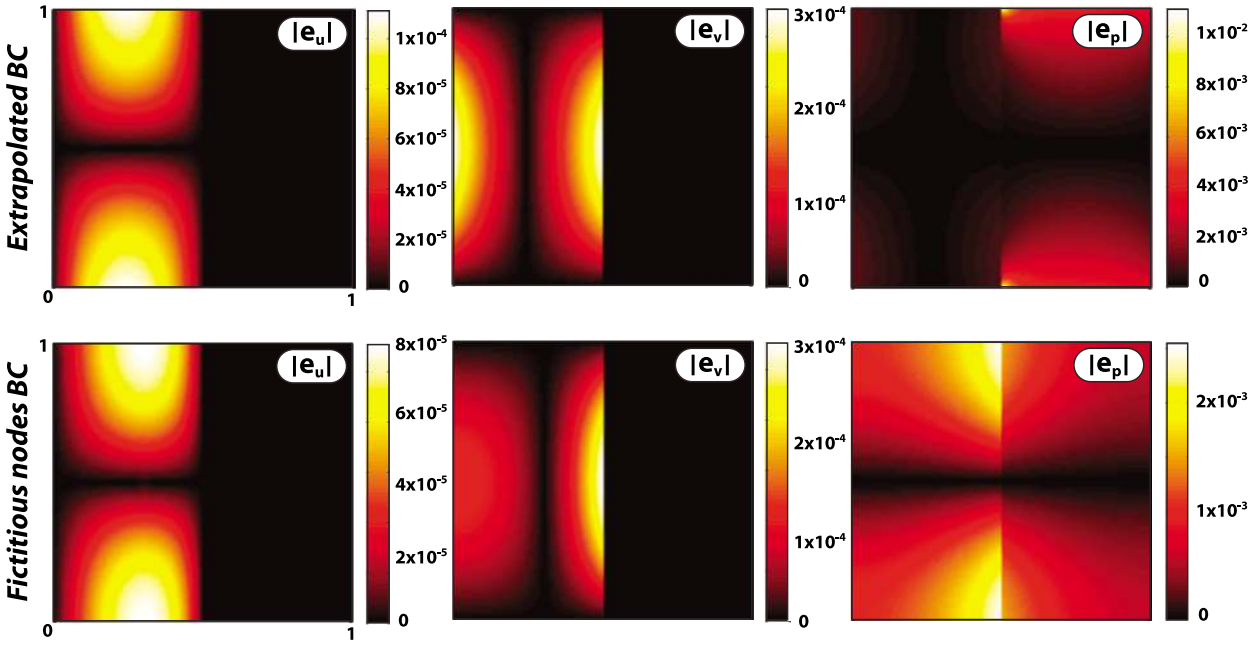

Figure 8. Absolute value of the discretization error for the primitive variables u, v, and p. Results are produced with the analytical solution SolCx with a viscosity jump of 10^6 and a grid resolution of 101 × 101 nodes. Extrapolated and fictitious node boundary condition implementations produce a similar velocity error pattern. The pressure error is dominant at the location of the viscosity jump.

from the markers onto the grid. The values of material properties at the cell center and cell vertices are calculated using the interpolation described by equation (10). We tested both the 1-cell and 4-cell interpolation schemes presented in section 2.2.1. In the following tests, we used an average of 64 markers per cell and we only considered using arithmetic viscosity averaging. In order to mimic the geometrically disturbed nature of an advected marker field, the markers were initially laid regularly throughout the grid and then perturbed such that each marker position $\mathbf{x}_p$ was randomly displaced (from the uniform distribution) by 1% of the grid spacing. The order of convergence in L_1 for velocity and pressure are reported in Table 2. Further tests (not shown here) indicated that these results are not sensitive to the perturbation applied to the markers' coordinates.

4.3.1. SolCx: Isoviscous

[45] The order of convergence for **u**, p in L_1 using different interpolation methods and the two boundary condition schemes are reported in Table 2. We note that both the 1-cell and 4-cell interpolation methods maintain the order of convergence in L_1 of the staggered grid discretization measured in section 4.2. In these isoviscous models, the style of boundary condition implementation influences the order of convergence of both the **u** and p fields. As in section 4.2, second-order boundary conditions show superiority by providing second-order convergence. While both marker interpolation methods provide

Table 2. Order of Convergence for the Coupled Staggered Grid and Marker-in-Cell Scheme Using an Arithmetic Viscosity Averaging and 64 Markers Per Cell[a]

	$\mathcal{I}$ (1-Cell)				$\mathcal{I}$ (4-Cell)			
	BC (First Order)		BC (Second Order)		BC (First Order)		BC (Second Order)	
	η^* (1)	η^* (10^6)	η^* (1)	η^* (10^6)	η^* (1)	η^* (10^6)	η^* (1)	η^* (10^6)
r_u	1.0309	1.0016	2.0115	1.0046	1.0344	1.0025	2.0122	1.0059
r_p	1.0323	1.0175	1.9875	1.009	1.0348	0.99797	2.0124	0.96827

[a]The results are produced using the analytical solution SolCx. They represent the rate at which the L_1 error norm decreases with increasing resolution. Comparison between two interpolation scheme ($\mathcal{I}$), two boundary condition implementations, and two different fluid viscosity contrasts (η^*).

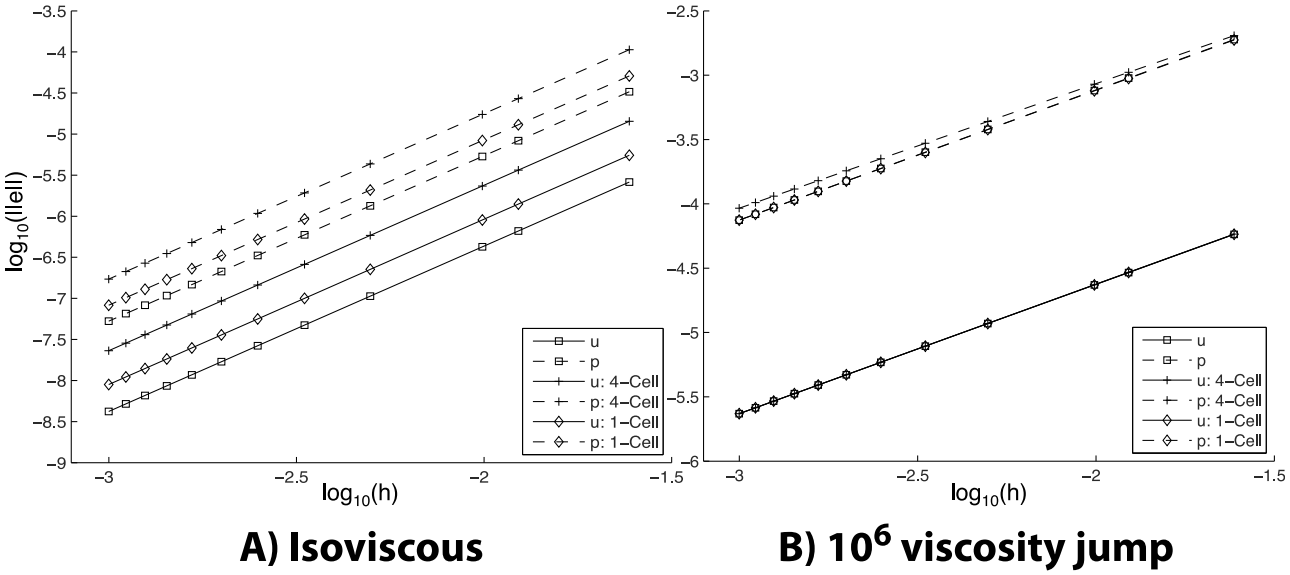

Figure 9. Velocity and pressure L_1 norms for SolCx test. Comparison of different material properties interpolations schemes (4-cell, 1-cell). Results are obtained using 64 markers per interpolation area. For this specific test, we used second-order BC. (a) With an isoviscous problem, velocity and pressure errors converge at second order. The offsets between the different lines are a result of the density interpolation. For similar marker density per interpolation volume, local interpolation provides more accurate results. (b) When a viscosity jump is introduced, all solutions converge at a first-order rate. The influence of the interpolation scheme is only noticeable on the pressure error.

similar rates of convergence, 1-cell interpolation is more accurate than 4-cell for a given number of marker per interpolation volume (Figure 9a). In this test, the viscosity field is spatially constant, thus the difference in error is therefore related to the interpolation of density (a smooth field in this model) required to assemble the force vector. The offsets between the velocity and pressure solutions with and without introducing marker-to-node interpolation is ~0.5 an order of magnitude.

4.3.2. SolCx: 10^6 Viscosity Jump

[46] In Figure 9b the errors for a sequence of grid resolutions used to solve the variable viscosity case are provided. Similarly to the test in section 4.2.2 in which no marker-to-node interpolation was employed, all the simulations converged with a rate of first order for velocity and pressure, regardless of the type of interpolation used. The choice of using either 1-cell or 4-cell interpolation method for interpolating the viscosity jump and the smoothly varying density field only appeared to affect the accuracy of the pressure field.

4.3.3. SolKz: 10^6 Smooth Viscosity Variation

[47] We have run the test SolKz to test the effect of a large continuous variation of viscosity through the domain. We have used second-order boundary conditions and two interpolation methods. Second-order L_1 velocity and pressure convergence were obtained while using 1-cell interpolation. 4-cell interpolation provided second-order velocity convergence and a pressure convergence order r_p, slightly less than 2. For this particular test, the absolute velocity and pressure error are approximately half an order of magnitude more accurate when the 1-cell method is utilized (Figure 10).

4.3.4. Inclusion Test: 10^3 Viscosity Jump

[48] This analytical solution requires a strain rate boundary condition (e.g., pure shear) to be applied far away from the center of the domain where the inclusion is located. In order to avoid any problems related to the treatment of this particular boundary condition, each boundary was treated as a Dirichlet boundary. The analytical solution was evaluated and imposed on the boundaries of our model domain. This approach also has the effect of removing the truncation error introduced while discretizing the strain rate boundary condition.

[49] The tests were run for an inclusion/bulk viscosity contrast of 10^3, using both the first-order and second-order boundary condition implementations. Nodal material properties were evaluated from the

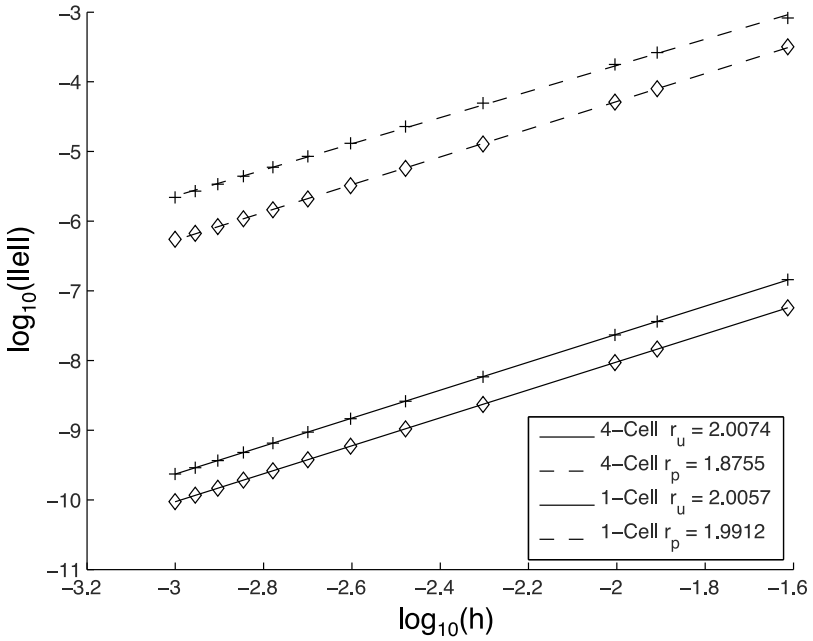

Figure 10. Dependance of L_1 velocity and pressure error norms on the grid spacing (h) for the SolKz test. We tested two different material properties interpolation (4-cell, 1-cell) with a fixed number of markers per interpolation volume (64). Second-order BC discretization were employed.

marker field using 1-cell and 4-cell interpolations and both interpolations were carried out using an average of 64 markers per interpolation volume. Given the sharp, two-dimensional viscosity structure (circular), this setup provides a tough test for both the discretization and the interpolation scheme. For all our cases, we obtained first-order convergence in L_1 for the velocity and pressure fields (Table 3).

4.3.5. Free Surface Stabilization

[50] In this section, we investigate the influence that the free surface stabilization scheme described in section 2.2.4 has on the order of convergence of the staggered grid discretization. For this purpose, we used the test SolCx described in section 4.1.1. This test does not include a free surface, but since the flow is driven by density gradients, the contribution of the stabilizing terms in the discretization is therefore nonzero. In order to choose the value of the time step, here we evaluate the time step using a Courant criteria (with $\theta = 0.5$) computed from the grid spacing and the maximum velocities given by the analytical solution. In practice, for time-dependent problems, the value of the time step used would be that computed from the flow field and mesh configuration from the previous time step.

[51] We ran a convergence test using the second-order boundary condition implementation and 1-cell interpolation (64 markers per interpolation volume) with a viscosity jump of 10^6. The stabilization affects the spatial distribution of error (compare Figure 11a with Figure 8). This affect is related to the proportionality between the magnitude of the correction term and the density gradients. With decreasing grid spacing, the numerical scheme with stabilization conserves its first-order convergence

Table 3. Order of Convergence for Velocity and Pressure for the Inclusion Test ($\eta^* = 10^3$), Using the Staggered Grid and Marker-in-Cell Scheme Employing an Arithmetic Viscosity Averaging and 64 Markers Per Cell[a]

	$\mathcal{I}$ (1-Cell)		$\mathcal{I}$ (4-Cell)	
	BC (First Order)	BC (Second Order)	BC (First Order)	BC (Second Order)
r_u	1.025	0.94897	1.0634	1.0043
r_p	0.98051	0.94107	0.99427	0.94204

[a]The order of convergence are observed to be independent of the type of marker-to-node interpolation and the style of boundary condition implementation.

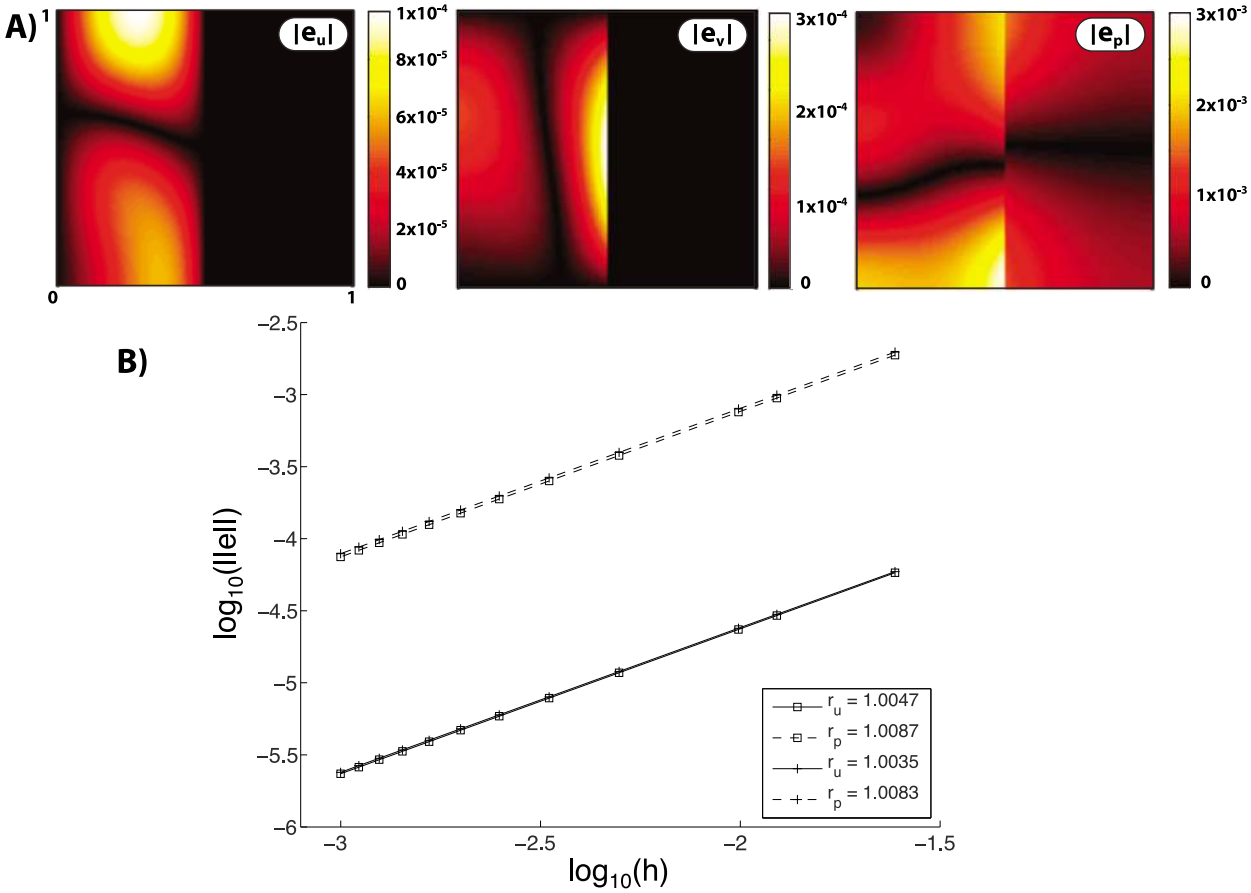

Figure 11. (a) Spatial distribution of the absolute value of the discretization error including the stabilization algorithm. (b) Influence of the stabilization algorithm on the convergence of the staggered grid and marker-in-cell discretization. The results were produced using the second-order BC and 1-cell interpolation (64 markers per cell); the setup includes a viscosity jump of 10^6. Dashed and solid lines are pressure and velocity L_1 convergence, respectively. Crosses represent the results obtained with the stabilization; squares are the reference results without stabilization.

in L_1 for both velocity and pressure, although a slight offset in pressure convergence was observed between simulations including or not the stabilization (dashed lines Figure 11b). Therefore the stabilization term does not noticeably modify the flow discretization, nor the overall convergence of the method.

5. Application to a Rayleigh-Taylor Instability With a Free Surface

[52] In section 4.3.5, we applied the free surface stabilization algorithm to the model setup of SolCx and observed that the order of convergence was unaltered by the introduction of the stabilization. We considered this test as being suitable for a convergence test, even though the problem does not include a free surface, as the flow is driven by buoyancy, thus possesses spatial variations in density. In order to test the robustness of the free surface stabilization scheme presented in section 2.2.4, we ran several simulations of a Rayleigh-Taylor instability with a free surface. This setup was used by *Kaus et al.* [2010] and was shown to produce the "drunken seaman" instability with a finite element code which explicitly tracked the free surface. With our Eulerian-Lagrangian approach, we approximate the free surface by using "sticky air", i.e., we introduce a layer of zero density, low-viscosity incompressible material [*Schmeling et al.*, 2008]. The pseudo free surface is then defined as the interface between the crust and the "sticky air", which is free to deform. The setup of the experiment consists of a domain $\Omega \equiv [-250, 250] \times [-600, 0]$ km, with a resolution of 50^2 cells (Δx = 10 km, Δy = 12 km). The box is filled with a 400 km thick asthenosphere, a 100 km thick layer

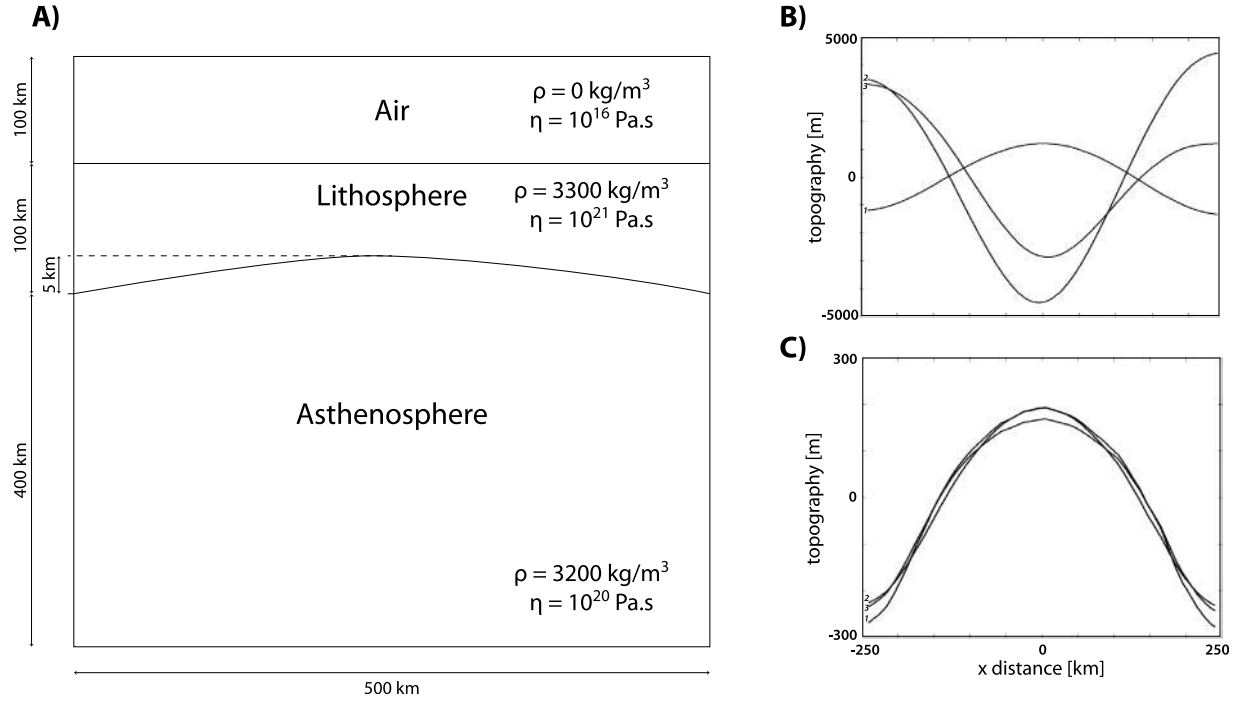

Figure 12. (a) Setup of the Rayleigh-Taylor instability with a free surface text (not to scale). (b) Example of early development of topography without stabilization with a Courant number equal to 0.5. Labels 1, 2, and 3 indicate topographic profiles at times 100, 167, and 171 kyr, respectively. The "drunken seaman" instability produces topography of very large amplitude that is not stable during time stepping. (c) Early development of topography with stabilization and Courant criteria equal to 0.5. The topographic signal is composed of a single positive topographic bulge in the center of the domain. Labels 1, 2, and 3 indicate topographic profiles at time 100, 200, and 300 kyr, respectively.

of lithosphere, and an additional 100 km thick layer of "sticky air" (Figure 12a). The lithosphere/asthenosphere interface is offset by a 5 km sinusoidal perturbation which is therefore a subgrid feature. The boundary conditions used are free slip at the top, left and right side of the domain, the bottom of the box is a no slip boundary. Omitting the stabilization scheme leads to the development of a surface instability from the very beginning of the experiment. The magnitude of the topography produced during the instability is unrealistically large and its polarity oscillates through time (Figure 12b). Including the stabilization enables the development of a stable topographic signal, characterized by a sinusoidal shape (Figure 12c). Following *Kaus et al.* [2010], we monitored the depth of the lithosphere/asthenosphere interface with time. In order to do so, we explicitly tracked the left most marker located on this interface, the results are reported in Figure 13. We tested the two different boundary condition implementations described in section 2.2.3. The results show that using the second-order boundary condition implementation enables our model to better reproduce the results of *Kaus et al.* [2010]. We suspect that the deviation observed using first-order boundary conditions witnesses of an accumulated (transport) error resulting from the nature of the BC implementation, affecting therefore the solution in the vicinity of the domain boundaries. In summary, the stabilization algorithm appears to effectively damp the oscillations that frequently arise when solving time-dependent problems which contain a strong density contrast. Despite the apparent stability of the algorithm when time steps defined by the classical Courant criterion are used, we note that, according to the timescale of interest, accurate topographic modeling may require the use of time steps which are much smaller than those predicted by the Courant criterion.

6. Perspectives

6.1. Improving Convergence Properties

[53] Throughout sections 4.2 and 4.3 we have observed the degradation of the order of convergence of the staggered grid solution when discontinuous viscosity structures were introduced. Figure 14 exhibits the decay of the L_1 velocity and pressure

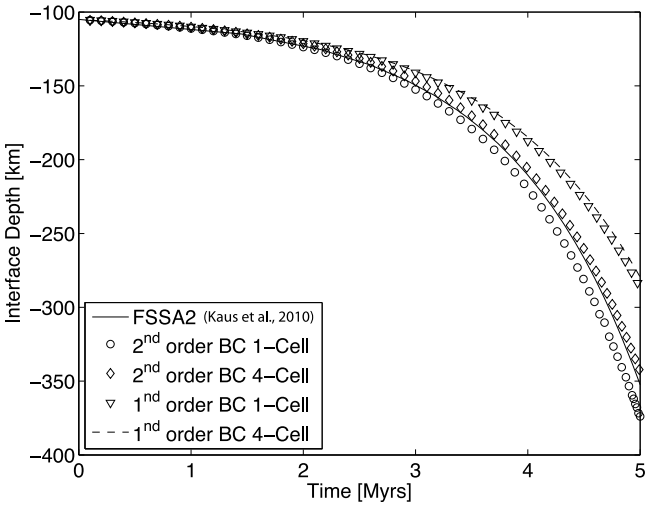

Figure 13. Free surface evolution during the Rayleigh-Taylor instability test as presented by *Kaus et al.* [2010]. We monitor the vertical coordinate of a marker initially positioned on the lithosphere/asthenosphere boundary and next to the left side of the box. Results are all computed for a Courant number equal to 0.5. Differences can been seen between the first-order and second-order boundary condition implementations; the latter follows the results [*Kaus et al.*, 2010] more closely.

convergence order with increasing viscosity contrast. Here we observe a reduction of the convergence, from second order to first order, when the viscosity contrast is increased from one (isoviscous) to ten. These results were obtained using the analytic solution SolCx. While these results are representative of a one-dimensional viscosity structure, this type of behavior is commonly observed when solving problems involving large discontinuities in coefficients [*Das et al.*, 1994], or waves such as those occurring in shock dynamics [*Banks et al.*, 2008], where shocks behaves as discontinuities and locally reduce the order of convergence of the numerical scheme. Restoring the optimal convergence properties of numerical method, prior to the introduction of the discontinuities is appealing. Here we briefly describe some efforts toward this.

[54] In section 4.2.2 we noted that under a specific alignment of our finite difference grid with the one-dimensional discontinuous viscosity structure, the optimal order of convergence for our method was observed. While this was regarded as a "special" case, it does raise the question, under what conditions is the viscosity jump correctly captured by our FD stencil? It has been proposed that different averaging methods (harmonic, geometric) of material properties can lead to improved numerical results [*MacKinnon and Carey*, 1988; *Das et al.*, 1994]. Examples of using such methods for viscous flow problems are available in the literature [*Das et al.*, 1994; *Deubelbeiss and Kaus*, 2008; *Schmeling et al.*, 2008], however, determining which averaging scheme is appropriate remains unsolved. The conclusions to this questions differ with the various model setup (boundary driven flow, buoyancy driven flow, viscosity contrast) and with the structure of the discontinuity (1-D versus 2-D versus 3-D geometries). While such averaging is completely justified in 1-D problems, it does not naturally generalize to higher dimensions and consequently is not robust enough for general use. Additionally, the aforementioned averaging methods only consider scalar quantities, or isotropic constitutive tensors. The extension of the approach to tensorial quantities, which may be required for obtaining an effective stress, or an effective orthotropic constitutive tensor is nontrivial. We refer to *Cowin and Yang* [1997] for further details on this topic.

[55] In contrast to rudimentary averaging of multiscale behavior (or coefficients), homogenization provides an alternative view by decomposing phenomena into two scales: a macroscale (coarse scale) and a microscale (fine scale). The essence of this class of methods is to extract coarse scale equations (or coefficients) which incorporate a multitude of different scales. The idea of scale separation can be naturally adopted to the FD-MIC scheme discussed here, in which we have a model domain discretized via cells (coarse scale) and within each cell we have numerous markers which define variations of the viscosity and density, thereby describing fine scale information. In classical homogenization theory [*Bensoussan et al.*,

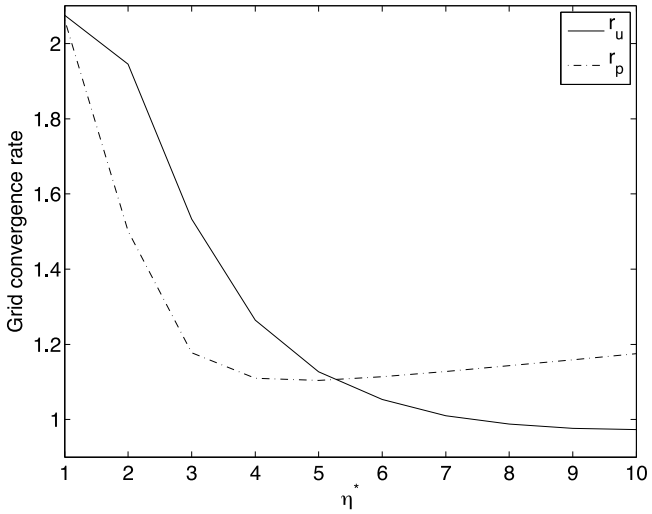

Figure 14. Measured convergence rate of the staggered grid with increasing viscosity contrast (η^*). Solid and dashed lines represent the convergence rate of the velocity and pressure measured in L_1, respectively. The measurements were carried out using the analytic solution SolCx and the second-order BC implementation. Projection of marker properties η, ρ was not used; these fields were evaluated on the FD stencil using equations (38) and (36).

1978; *Murat*, 1978], it is frequently required to assume that the fine scale heterogeneity is periodic in one direction, thus this approach may lack the generality required. Nevertheless, further extensions of classical homogenization are being developed for nonperiodic heterogeneities [*Capdeville et al.*, 2010]. For a thorough review of homogenization we refer to *Hassani and Hinton* [1998a, 1998b, 1998c]. Numerous alternatives to classical homogenization exist [see, e.g., *Brewster and Beylkin*, 1995; *Abdulle and Weinan*, 2003; *Arbogast*, 2002; *Jenny et al.*, 2003; *Weinan and Engquist*, 2003; *Kouznetsova et al.*, 2002]. These methods also employ coarse and fine scale representation of the problem, however they do not assume that the fine structure is periodic. Many of these methods require the solution of independent cell problems, where local, fine scale solutions are subsequently coupled to a coarse grid solution. Such approaches could used in geodynamic models to resolve fine scale structure defined via the markers, and may also improve the convergence [*Masud and Khurram*, 2004; *Liu and Li*, 2006] of our scheme in the presence of discontinuous viscosity fields.

6.2. Input Data Uncertainty Estimation and Model Parameter Sensitivity

[56] In the light of establishing that the numerical scheme employed to solve a given set of equations, which describes the geodynamic process of interest, has been deemed to be sufficiently accurate and robust, other challenges await. Geodynamic simulations require prescription of the rheological behavior and its associated parameters for each lithology present in the system. In practice, these parameters and flow laws are frequently derived experimentally. The evaluation of flow parameters at high pressure/temperature is a challenging task and the behavior of crystals such as olivine at depth still remains widely debated [*Raterron et al.*, 2009; *Rozel et al.*, 2011]. Moreover, the extrapolation of flow laws from laboratory time scales to geological time scales give rise to additional uncertainties [*Paterson*, 1987]. One interesting direction for geodynamic modeling is the integration of the material property uncertainties into the simulations, as done in other communities [*Laz et al.*, 2007; *Houtekamer et al.*, 1996; *Rabier et al.*, 1996].

[57] Another avenue to explore could be to consider the geodynamic model as an "optimal design" problem [*Hicks and Henne*, 1978; *Jameson*, 1988, 1995; *Giles and Pierce*, 2000]. In such approaches, one seeks to minimize (or maximize) a given objective function F, subject to set of design variables $\mathbf{U}$ which define the model setup. For instance, in the context of a viscous folding model, the design parameters might be: size of the model domain, rheological parameters (viscosity, density), rate of compression applied as a boundary condition, and the objective function could be to minimize the difference between the dominant

wavelength from the model and one observed from field data. From such optimal design approaches, one obtains the relativity sensitivity of F with respect to each design parameter U_i, or phrased another way, we can answer the question of what is the perturbation in dominant wavelength due the domain size, rheological parameters and boundary condition. Both optimal design and the integration of parameter uncertainties provide a means to quantitatively characterize model parameter sensitivities, thereby further developing our understanding of the system of equations we choose to represent our geological problem.

7. Conclusions

[58] Computational modeling in geology requires numerical methods that are robust, reliable and accurate when applied to study the deformation of materials which possess discontinuities in their properties. Such variations in material parameters are likely to strongly influence the quality of the solution. While theoretical analysis of such methods is difficult due to the discontinuous nature of the material properties, very few numerical studies focussing specifically on the quality of discrete solutions obtained from geodynamic models have been performed. Quantifying the numerical accuracy for complex models that are relevant to geodynamics is of vital importance if the solution are to be used in any quantitative manner. In this study, we address these issues by examining the discretization errors and convergence characteristics of the discrete solution obtained from the FD-MIC scheme, which is a widely utilized method in the geodynamic community.

[59] The convergence study was carried out using two-dimensional analytical solutions which possess large continuous and discontinuous variations in the viscosity field. Two different boundary conditions implementations, namely extrapolated BC and fictitious nodes methods were tested. If the fluid was isoviscous, we found that the fictitious node method provided second-order accurate velocity and pressure fields and therefore showed superiority over the extrapolated BC method, which produced first-order accurate fields. Smooth but large variations of viscosity throughout the model domain did not affect the second-order behavior of the FD-MIC method. However, the introduction of a viscosity jump in the model domain affected the convergence properties of the fictitious node method, resulting in first-order velocity and pressure fields. This drop in the order of convergence occurred if the viscosity jump was larger than 5. An essential component of our Eulerian-Lagrangian discretizations is the projection of marker properties onto the finite difference grid. We tested two different marker-to-node projections which differ in their domain of influence. Introducing these projections was not observed to modify the order of convergence of the FD-MIC method. The more local 1-cell interpolation was shown to be more accurate than the 4-cell interpolation. For the range of problems considered, our results clearly establish that the FD-MIC scheme converges. That is, increases in the numerical resolution lead to a reduction of the discretization error. Demonstrating that the method is convergent adds robustness to both previous and future geodynamic applications which employ this particular numerical method.

[60] Additionally, we introduced a strong form variant of the free surface stabilization algorithm presented by *Kaus et al.* [2010]. This stabilization method is suitable for finite difference discretizations. By the means of a convergence test, we showed that the stabilization algorithm also does not notably affect the convergence properties of our numerical scheme. Further testing was carried out by performing time-dependent simulations and using a setup which is prone to instability. This test demonstrated that the stabilization suppresses the instability that may occur while running free surface calculations. The stabilization permits larger time steps to be used. Whilst this certainly does not improve the temporal accuracy of the solution, its inclusion is necessary to obtain physically meaningful results from simulations which use a Courant time step. The stabilization method is important for any simulation that includes large density contrasts. In our modeling, the surface of the Earth is a classical example of this type of interface. Thus, this stabilization routine approach is particularly relevant for modeling topography in regional and global scale simulations over geological time periods.

[61] Lastly, we wish to remark that continued research in understanding discretization errors and convergence properties of the numerical tools used to study geological processes is vitally important if we wish to develop the level of reliability and robustness in our modeling technology which exists in the engineering community. However, equally as important as the quality of our numerical solutions, is our ability to understand the dynamics of the system we use to describe geological processes, and this entails understanding the sensitivity of the model output to the underlying flow laws, material

parameters and boundary conditions and other input used to define our model.

Acknowledgments

[62] The authors thank Harro Schmeling and Cedric Thieulot for constructive reviews that improved the quality and clarity of the paper. We also thank Jed Brown and Alban Souche for useful discussions related to the free surface stabilization and discretization errors. We thank Boris Kaus for constructive input and fruitful discussions related to errors and for providing the Matlab script defining the analytical solution for the viscous inclusion test and data for the Rayleigh-Taylor test. DAM acknowledges Mirko Vélic for producing the source code used to evaluate the analytic solution, SolCx and SolKz. TD thanks la Tartouze for proofreading. TD was funded by the SNF-EU research grant 20TO21-120535 (TOPO-4D). DAM was supported by the ETH Zurich Postdoctoral Fellowship Program.

References

Abdulle, A., and E. Weinan (2003), Finite difference heterogeneous multi-scale method for homogenization problems, *J. Comput. Phys.*, *191*, 18–39.

Arbogast, T. (2002), Implementation of a locally conservative numerical subgrid upscaling scheme for two-phase Darcy flow, *Comp. Geosci.*, *6*, 453–481.

Babeyko, A. Y., S. V. Sobolev, R. B. Trumbull, O. Oncken, and L. L. Lavier (2002), Numerical models of crustal-scale convection and partial melting beneath the Altiplano-Puna plateau, *Earth Planet. Sci. Lett.*, *199*, 373–388.

Banks, J. W., T. Aslam, and W. J. Rider (2008), On sub-linear convergence for linearly degenerate waves in capturing schemes, *J. Comput. Phys.*, *227*, 6985–7002.

Bensoussan, A., J. Lions, and G. Papanicolau (1978), *Asymptotic Analysis for Periodic Structures*, 700 pp., North Holland, Amsterdam.

Blankenbach, B., F. Busse, U. Christensen, L. Cserepes, D. Gunkel, U. Hansen, H. Harder, G. Jarvis, M. Koch, G. Marquart, D. Moore, P. Olson, H. Schmeling, and T. Schnaubelt (1989), A benchmark comparison for mantle convection codes, *Geophys. J. Int.*, *98*, 23–38.

Braun, J., and M. Sambridge (1994), Dynamical Lagrangian Remeshing (DLR): A new algorithm for solving large strain deformation problems and its application to fault-propagation folding, *Earth Planet. Sci. Lett.*, *124*, 211–220.

Braun, J., and M. Sambridge (1995), A numerical method for solving partial differential equations on highly irregular evolving grids, *Nature*, *376*, 655–660.

Braun, J., C. Thieulot, P. Fullsack, M. DeKool, C. Beaumont, and R. Huismans (2008), DOUAR: A new three-dimensional creeping flow numerical model for the solution of geological problems, *Phys. Earth Planet. Inter.*, *171*(1–4), 76–91.

Brewster, M. E., and G. Beylkin (1995), A multiresolution strategy for numerical homogenization, *Appl. Comput. Harmonic Anal.*, *2*(4), 327–349.

Buiter, S. J. H., A. Y. Babeyko, S. Ellis, T. V. Gerya, B. J. P. Kaus, A. Kellner, G. Schreurs, and Y. Yamada (2006), Analogue benchmarks of shortening and extension experiments, in *Analogue and Numerical Modelling of Crustal-Scale Processes*, edited by S. J. H. Buiter and G. Schreurs, *Geol. Soc. Spec. Publ.*, *253*, 1–27.

Capdeville, Y., L. Guillot, and J.-J. Marigo (2010), 2-D non-periodic homogenization to upscale elastic media for P-SV waves, *Geophys. J. Int.*, *182*(2), 903–922.

Cowin, S. C., and G. Yang (1997), Averaging anisotropic elastic constant data, *J. Elasticity*, *46*, 151–180.

Das, B., S. Steinberg, D. Zhang, and T. Robey (1994), Comparisons of numerical solution methods for differential equations with discontinuous coefficients, *Mathematics and Computers in Simulation*, *40*, 57–75.

Deubelbeiss, Y., and B. J. P. Kaus (2008), Comparison of Eulerian and Lagrangian numerical techniques for the Stokes equations in the presence of strongly varying viscosity, *Phys. Earth Planet. Inter.*, *171*, 92–111.

Fuchs, L., H. Schmeling, and H. Koyi (2011), Numerical models of salt diapir formation by down-building: The role of sedimentation rate, viscosity contrast, initial amplitude, and wavelength, *Geophys. J. Int.*, doi:10.1111/j.1365-246X.2011.05058.x, in press.

Fullsack, P. (1995), An arbitrary Lagrangian-Eulerian formulation for creeping flows and its application in tectonic models, *Geophys. J. Int.*, *120*, 1–23.

Gerya, T. V. (2010), *Introduction to Numerical Geodynamic Modelling*, 345 pp., Cambridge Univ. Press, Cambridge, UK.

Gerya, T. V., and D. A. Yuen (2003), Characterictics-based marker method with conservative finite-difference schemes for modeling geological flows with strongly variable transport properties, *Phys. Earth Planet. Inter.*, *140*(4), 293–318.

Gerya, T. V., and D. A. Yuen (2007), Robust characteristics method for modelling multiphase visco-elasto-plastic thermo-mechanical problems, *Phys. Earth Planet. Inter.*, *163*, 83–105.

Giles, M., and N. Pierce (2000), An introduction to the adjoint approach to design, *Flow, Turbul. Combust.*, *65*, 393–415.

Hansen, D. (2003), A meshless formulation for geodynamic modeling, *J. Geophys. Res.*, *108*(B11), 2549, doi:10.1029/2003JB002460.

Harder, H., and U. Hansen (2005), A finite-volume solution method for thermal convection and dynamo problems in spherical shells, *Geophys. J. Int.*, *161*, 522–532.

Harlow, F. H., and E. Welch (1965), Numerical calculation of time-dependent viscous flow of fluid with free surface, *Phys. Fluids*, *8*(12), 2182–2189.

Hassani, B., and E. Hinton (1998a), A review of homogenization and topology optimization I–homogenization theory for media with periodic structure, *Comput. Struct.*, *69*(6), 707–717.

Hassani, B., and E. Hinton (1998b), A review of homogenization and topology opimization II–analytical and numerical solution of homogenization equations, *Comput. Struct.*, *69*(6), 719–738.

Hassani, B., and E. Hinton (1998c), A review of homogenization and topology optimization III–topology optimization using optimality criteria, *Comput. Struct.*, *69*(6), 739–756.

Hicks, R., and P. Henne (1978), Wing design by numerical optimization, *J. Aircr.*, *15*(7), 407–412.

Houtekamer, P., L. Lefaivre, J. Derome, H. Ritchie, and H. Mitchell (1996), A system simulation approach to ensemble prediction, *Mon. Weather Rev.*, *124*(6), 1225–1242.

Jameson, A. (1988), Aerodynamic design via control theory, *J. Sci. Comput.*, *3*, 233–260.

Jameson, A. (1995), Optimum aerodynamic design using CFD and control theory, *Tech. Rep. AIAA95-1729-CP*, Dep. of Mech. and Aerosp. Eng., Princeton Univ., Princeton, N. J.

Jenny, P., S. H. Lee, and H. A. Tchelepi (2003), Multi-scale finite-volume method for elliptic problems in subsurface flow simulation, *J. Comp. Phys.*, *187*(1), 47–67.

Katz, R., M. Knepley, B. Smith, M. Spiegelman, and E. Coon (2007), Numerical simulation of geodynamic processes with the portable extensible toolkit for scientific computation, *Phys. Earth Planet. Inter.*, *163*(1–4), 52–68.

Kaus, B. J. P., H. Mühlhaus, and D. A. May (2010), A stabilization algorithm for geodynamic numerical simulations with a free surface, *Phys. Earth Planet. Inter.*, *181*, 12–20.

Kouznetsova, V., M. Geers, and W. Brekelmans (2002), Multi-scale constitutive modelling of heterogeneous materials with a gradient-enhanced computational homogenization scheme, *Int. J. Numer. Methods Eng.*, *54*(8), 1235–1260.

Laz, P. J., J. Q. Stowe, M. A. Baldwin, A. J. Petrella, and P. J. Rullkoetter (2007), Incorporating uncertainty in mechanical properties for finite element-based evaluation of bone mechanics, *J. Biomech.*, *36*, 2831–2836.

Lin, S.-C., and P. E. van Keken (2006), Dynamics of thermochemical plumes: 1. Plume formation and entrainment of a dense layer, *Geochem. Geophys. Geosyst.*, *7*, Q02006, doi:10.1029/2005GC001071.

Liu, X., and S. Li (2006), A variational multiscale stabilized finite element method for the Stokes flow problem, *Finite Elem. Anal. Des.*, *42*, 580–591.

MacKinnon, R. J., and G. F. Carey (1988), Analysis of material interface discontinuities and superconvergent fluxes in finite difference theory, *J. Comput. Phys.*, *75*(1), 151–167.

Masud, A., and R. Khurram (2004), A multiscale/stabilized finite element method for the advection-diffusion equation, *Comput. Methods Appl. Mech. Eng.*, *193*, 1997–2018.

Moresi, L., S. Zhong, and M. Gurnis (1996), The accuracy of finite element solutions of Stokes' flow with strongly varying viscosity, *Phys. Earth Planet. Inter.*, *97*(1–4), 83–94.

Moresi, L., F. Dufour, and H.-B. Mühlhaus (2003), A Lagrangian integration point finite element method for large deformation modeling of viscoelastic geomaterials, *J. Comput. Phys.*, *184*, 476–497.

Moresi, L., S. Quenette, V. Lemiale, C. Meriaux, B. Appelbe, and H. Mühlhaus (2007), Computational approaches to studying non-linear dynamics of the crust and mantle, *Phys. Earth Planet. Inter.*, *163*, 69–82.

Murat, F. (1978), Compacité par compensation, *Ann. Sc. Norm. Super. Pisa CI. Sci.*, *5*(4), 489–507.

Nicolaides, R. A. (1992), Analysis and convergence of the MAC scheme. I. The linear problem, *SIAM J. Numer. Anal.*, *29*(6), 1579–1591.

Nicolaides, R. A., and X. Wu (1996), Analysis and convergence of the MAC scheme. II. Navier-Stokes equations, *Math. Comput.*, *65*(213), 29–44.

Ogawa, M., G. Schubert, and A. Zebib (1991), Numerical simulations of three-dimensional thermal convection in a fluid with strongly temperature-dependent viscosity, *J. Fluid Mech.*, *233*, 299–328.

OzBench, M., K. Regenauer-Lieb, D. R. Stegman, G. Morra, R. Farrington, A. Hale, D. A. May, J. Freeman, L. Bourgouin, H. Mühlhaus, and L. Moresi (2008), A model comparison study of large-scale mantle-lithosphere dynamics driven by subduction, *Phys. Earth Planet. Inter.*, *171*, 224–234.

Patankar, S. (1980), *Numerical Heat Transfer and Fluid Flow*, 192 pp., Hemisphere, Washington, D. C.

Paterson, M. S. (1987), Problems in the extrapolation of laboratory rheological data, *Tectonophysics*, *133*(1–2), 33–43.

Poliakov, A., and Y. Podladchikov (1992), Diapirism and topography, *Geophys. J. Int.*, *109*, 553–564.

Poliakov, A., P. Cundall, Y. Podladchikov, and V. Lyakhovsky (1993), An explicit inertial method for the simulation of the viscoelastic flow: An evaluation of elastic effects on diapiric flow in two- and three-layer models, in *Flow and Creep in the Solar System: Observations, Modelling and Theory*, edited by D. Stone and S. Runcorn, pp. 175–195, Kluwer Acad., Dordrecht, Netherlands.

Popov, A., and S. Sobolev (2008), SLIM3D: A tool for three-dimensional thermomechanical modeling of lithospheric deformation with elasto-visco-plastic rheology, *Phys. Earth Planet. Inter.*, *171*(1–4), 55–75, doi:10.1016/j.pepi. 2008.03.007.

Pracht, W. E. (1971), A numerical method for calculating transient creep flows, *J. Comput. Phys.*, *7*, 46–60.

Rabier, F., E. Klinker, P. Courtier, and A. Hollingsworth (1996), Sensitivity of forecast errors to initial conditions, *Q. J. R. Meteorol. Soc.*, *122*, 121–150.

Ratcliff, J. T., G. Schubert, and A. Zebib (1995), Three-dimensional variable viscosity convection of an infinite Prandtl number Boussinesq fluid in a spherical shell, *Geophys. Res. Lett.*, *22*(16), 2227–2230.

Raterron, P., E. Amiguet, J. Chen, L. Li, and P. Cordier (2009), Experimental deformation of olivine single crystals at mantle pressures and temperatures, *Phys. Earth Planet. Inter.*, *172*(1–2), 74–83.

Revenaugh, J., and B. Parsons (1987), Dynamic topography and gravity anomalies for fluid layers whose viscosity varies exponentially with depth, *Geophys. J. R. Astron. Soc.*, *90*, 349–368.

Roache, P. J. (1997), Quantification of uncertainty in computational fluid dynamics, *Annu. Rev. Fluid. Mech.*, *29*, 123–160.

Roy, C. J. (2010), Review of discretization error estimators in scientific computing, paper presented at 48th AIAA Aerospace Sciences Meeting Including the New Horizons Forum and Aerospace Exposition, Orlando, Fla., 4–7 Jan.

Rozel, A., Y. Ricard, and D. Bercovici (2011), A thermodynamically self-consistent damage equation for grain size evolution during dynamic recrystallization, *Geophys. J. Int.*, *184*(2), 719–728.

Samuel, H., and M. Evonuk (2010), Modeling advection in geophysical flows with particle level sets, *Geochem. Geophys. Geosyst.*, *11*, Q08020, doi:10.1029/2010GC003081.

Schmalzl, J., and A. Loddoch (2003), Using subdivision surfaces and adaptive surface simplification algorithms for modeling chemical heterogeneities in geophysical flows, *Geochem. Geophys. Geosyst.*, *4*(9), 8303, doi:10.1029/2003GC000578.

Schmeling, H., A. Y. Babeyko, A. Enns, C. Faccenna, F. Funiciello, T. V. Gerya, G. J. Golabek, S. Grigull, B. J. P. Kaus, G. Morra, S. M. Schmalholz, and J. van Hunen (2008), A benchmark comparison of spontaneous subduction models–Towards a free surface, *Phys. Earth Planet. Inter.*, *171*(1–4), 198–223.

Schmid, D. W. (2002), Finite and infinite heterogeneities under pure and simple shear, Ph.D. thesis, ETH Zurich, Zurich, Switzerland.

Schmid, D. W., and Y. Y. Podladchikov (2003), Analytical solutions for deformable elliptical inclusions in general shear, *Geophys. J. Int.*, *155*, 269–288.

Schwaiger, H. F. (2007), An implementation of smoothed particle hydrodynamics for large deformation, history dependent geomaterials with applications to tectonic deformation, Ph.D. thesis, Univ. of Wash., Seattle.

Stemmer, K., H. Harder, and U. Hansen (2006), A new method to simulate convection with strongly temperature- and pressure-

dependent viscosity in a spherical shell: Applications to the Earth's mantle, *Phys. Earth Planet. Inter.*, *157*(3–4), 223–249.

Tackley, P. J. (1993), Effects of strongly temperature-dependent viscosity on time-dependent, three-dimensional models of mantle convection, *Geophys. Res. Lett.*, *20*, 2187–2190.

Tackley, P. J. (1998), Three-dimensional simulations of mantle convection with a thermo-chemical basal boundary layer: D″?, in *The Core-Mantle Boundary Region*, *Geophys. Monogr. Ser.*, vol. 28, edited by M. Gurnis, pp. 231–253, AGU, Washington, D. C.

Tackley, P. J. (2008), Modelling compressible mantle convection with large viscosity contrasts in a three-dimensional spherical shell using the yin-yang grid, *Phys. Earth Planet. Inter.*, *171*(1–4), 7–18.

Tackley, P. J., and S. D. King (2003), Testing the tracer ratio method for modeling active compositional fields in mantle convection simulations, *Geochem. Geophys. Geosyst.*, *4*(4), 8302, doi:10.1029/2001GC000214.

Travis, B. J., C. Anderson, J. Baumgardner, C. W. Gable, B. H. Hager, R. J. O'Connell, P. Olson, A. Raefsky, and G. Schubert (1990), A benchmark comparison of numerical methods for infinite Prandtl number thermal convection in two-dimensional Cartesian geometry, *Geophys. Astrophys. Fluid Dyn.*, *55*, 137–160.

Trompert, R. A., and U. Hansen (1996), The application of a finite volume multigrid method to three-dimensional flow problems in a highly viscous fluid with a variable viscosity, *Geophys. Astrophys. Fluid Dyn.*, *83*(3), 261–291.

van Keken, P. E., S. D. King, H. Schmeling, U. R. Christensen, D. Neumeister, and M.-P. Doin (1997), A comparison of methods for the modeling of thermochemical convection, *J. Geophys. Res.*, *102*, 22,477–22,496.

van Keken, P. E., C. Currie, S. D. King, M. D. Behn, A. Cagnioncle, J. He, R. F. Katz, S.-C. Lin, E. M. Parmentier, M. Spiegelman, and K. Wang (2008), A community benchmark for subduction zone modeling, *Phys. Earth Planet. Inter.*, *171*(1–4), 187–197.

Weinan, E., and B. Engquist (2003), The heterogeneous multi-scale methods, *Comm. Math. Sci.*, *1*, 87–133.

Weinberg, R. F., and H. Schmeling (1992), Polydiapirs: Multi-wave length gravity structures, *J. Struct. Geol.*, *14*, 425–436.

Zaleski, S., and P. Julien (1992), Numerical simulation of Rayleigh-Taylor instability for single and multiple salt diapirs, *Tectonophysics*, *206*(1–2), 55–69.

Zhong, S. (1996), Analytic solutions for Stokes' flow with lateral variations in viscosity, *Geophys. J. Int.*, *124*, 18–28.

Zhong, S., A. McNamara, E. Tan, L. Moresi, and M. Gurnis (2008), A benchmark study on mantle convection in a 3-D spherical shell using CitcomS, *Geochem. Geophys. Geosyst.*, *9*, Q10017, doi:10.1029/2008GC002048.

Zlotnik, S., P. Díez, M. Fernández, and J. Vergés (2007), Numerical modelling of tectonic plates subduction using X-FEM, *Comput. Methods Appl. Mech. Eng.*, *196*, 4283–4293.